



HAL
open science

Tropical cyclones in global high-resolution simulations using the IPSL model

Stella Bourdin, Sébastien Fromang, Arnaud Caubel, Josefine Ghattas, Yann Meurdesoif, Thomas Dubos

► **To cite this version:**

Stella Bourdin, Sébastien Fromang, Arnaud Caubel, Josefine Ghattas, Yann Meurdesoif, et al.. Tropical cyclones in global high-resolution simulations using the IPSL model. *Climate Dynamics*, 2024, 10.1007/s00382-024-07138-w . hal-04574670

HAL Id: hal-04574670

<https://hal.science/hal-04574670>

Submitted on 14 May 2024

HAL is a multi-disciplinary open access archive for the deposit and dissemination of scientific research documents, whether they are published or not. The documents may come from teaching and research institutions in France or abroad, or from public or private research centers.

L'archive ouverte pluridisciplinaire **HAL**, est destinée au dépôt et à la diffusion de documents scientifiques de niveau recherche, publiés ou non, émanant des établissements d'enseignement et de recherche français ou étrangers, des laboratoires publics ou privés.



Tropical cyclones in global high-resolution simulations using the IPSL model

Stella Bourdin¹ · Sébastien Fromang¹ · Arnaud Caubel¹ · Josefine Ghattas² · Yann Meurdesoif¹ · Thomas Dubos³

Received: 5 August 2023 / Accepted: 25 January 2024
© The Author(s) 2024

Abstract

Despite many years of extensive research, the evolution of Tropical Cyclone (TC) activity in our changing climate remains uncertain. This is partly because the answer to that question relies primarily on climate simulations with horizontal resolutions of a few tens of kilometers. Such simulations have only recently become accessible for most modeling centers, including the Institut Pierre-Simon Laplace (IPSL). Using recent numerical developments in the IPSL model, we perform a series of historical atmospheric-only simulations that follow the HighResMIP protocol. We assess the impact of increasing the resolution from ~ 200 to 25 km on TC activity. In agreement with previous work, we find a systematic improvement of TC activity with increasing resolution with respect to the observations. However, a clear signature of TC frequencies convergence with resolution is still lacking. Cyclogenesis geographical distributions also improve at the scale of individual basins. This is particularly true of the North Atlantic, where the agreement with the observed distribution is impressive at 25 km. In agreement with the observations, TC activity correlates with the large-scale environment and ENSO in that basin. By contrast, TC frequencies remain too small in the Western North Pacific at 25 km, where significant biases of humidity and vorticity are found compared to the reanalysis. Despite the few minor weaknesses we identified, our results demonstrate that the IPSL model is a suitable tool for studying TCs on climate time scales. This work thus opens the way for further studies contributing to our understanding of TC climatology.

Keywords Tropical cyclones · Climate model · IPSL · Resolution · Variability

1 Introduction

Tropical Cyclones (TCs) are the deadliest and costliest non-geological natural disaster. They account for 38% of disaster-related human and economic losses between 1970 and 2019, according to WMO (2023). Yet, much uncertainty remains regarding how cyclonic activity will evolve with climate change, even compared to other extreme events. There are several reasons why the understanding of tropical cyclone climatology is lagging, despite extensive research. First,

the span of reliable observations is short—about forty years since the advent of satellite imagery (Knapp et al. 2018). Second, as detailed below, it is difficult to simulate tropical cyclones in numerical climate models (Camargo and Wing 2016). Lastly, and to some extent for the first two reasons, despite extensive research and a broad agreement about the most important processes at work, there remains gaps in our understanding of TC genesis, structure, and lifecycle (Emanuel 2018; Smith and Montgomery 2023).

Simulating tropical cyclones in climate models is a challenging problem for three reasons: first, horizontal resolution, which is crucial to resolving tropical cyclones' structures and intensities, is a limiting factor for most modeling centers; second, simulated tropical cyclones are sensitive to several different parameterizations (e.g., Nardi et al. 2022a; Zarzycki et al. 2021; Lim et al. 2015); finally, dynamical core formulation might play a role (Reed et al. 2015). The role of resolution is the main focus of the present paper.

Extensive research has indeed demonstrated its crucial role in simulating tropical cyclones adequately. The recent

✉ Stella Bourdin
stella.bourdin@lsce.ipsl.fr

¹ Laboratoire des Sciences du Climat et de l'Environnement (LSCE-IPSL) CEA-CNRS-UVSQ-Université Paris Saclay, 91190 Gif-sur-Yvette, France

² Institut Pierre Simon Laplace (IPSL), Sorbonne Université-CNRS, 75000 Paris, France

³ Laboratoire de Météorologie Dynamique (LMD-IPSL), Ecole Polytechnique, 91120 Palaiseau, France

High-Resolution Model Intercomparison Project (HighResMIP, Haarsma et al. 2016) provided a multi-model ensemble of high-resolution global multi-decadal simulations. The results published by Roberts et al. (2020) are representative of the state of the art: increasing resolution allows the simulation of more frequent and more intense tropical cyclones with better geographical distribution relative to observations. They confirm, in particular, the results obtained by the U.S. CLIVAR Hurricane Working Group (HWG) (Wehner et al. 2015; Walsh et al. 2015). Other aspects of TC climatology sensitivity to resolution have been investigated using the HighResMIP ensemble. Regarding precipitation in particular, Zhang et al. (2021) showed that the global TC-related precipitation distribution systematically improves with resolution, but contrasting results were obtained regarding changes in per-TC precipitation (Vanni re et al. 2020; Moon et al. 2020). Although the focus of HighResMIP is resolution and not climate change, it could have been that improving TC representations helped with climate change projections. However, Roberts et al. (2020) did not find a consistent prediction of TC frequency and intensity evolutions with climate change in the HighResMIP ensemble.

Orthogonally to multi-model approaches, several studies have used one model at different resolutions. Manganello et al. (2012) used the ECMWF IFS at resolutions up to 10 km and analyzed northern hemisphere TCs over 30 years. Strachan et al. (2013) investigated resolution sensitivity from 3.75  to 0.55  with HadGEM1, and Roberts et al. (2015) from 130 to 25 km with UKMO GA3. The results from these studies are in line with multi-model approaches: increasing resolution increases TCs frequency and intensity and improves their geographical distribution. Using only one model and several resolutions also allows to provide more precise insights concerning the effect of spatial resolution and the necessary resolution required to simulate TC climatology adequately. In particular, when resolution is increased, Roberts et al. (2015) show improved TC structures with a reduced radius of maximum winds (RMW). Manganello et al. (2012) highlights that TCs interannual variability better compares to observations. There are discrepancies, however, regarding the resolution deemed appropriate for adequate simulations of TC statistics. Strachan et al. (2013) concludes that 135 km is sufficient to simulate TC frequency and 100 km for interannual variability, whereas Manganello et al. (2012) and Roberts et al. (2015) did not find any hints that TC frequencies converge in their range of resolution. Because of limited computational power, one limit of these studies is their duration of integration, which is thirty years or less.

This quick overview of the current state of the art of high-resolution TC modeling highlights the field's current limitations and the need for more work. Only a limited number of climate models have been run at high enough resolution

to investigate TCs statistical properties directly, and their conclusions sometimes differ, as described above for the issue of convergence. More studies are needed to increase our confidence in the results of high-resolution simulations and projections.

Our paper takes place in this context and aims to contribute to the community's recent efforts regarding these issues. It builds upon recent numerical developments in the Institut Pierre-Simon Laplace (IPSL) earth system model. First, there have been significant improvements in the atmospheric parametrizations between the CMIP5 and CMIP6 campaigns (Hourdin et al. 2020). In addition, a new dynamical core, called DYNAMICO, has recently been developed (Dubos et al. 2015) and can now be used along with the other components of the IPSL earth system model. Of particular interest for the present paper is the fact that DYNAMICO uses an icosahedral grid that enables high-resolution simulations to be completed in a reasonable time due to increased parallelism. DYNAMICO has already been used to study Saturn atmospheric dynamics at high resolution (Spiga et al. 2020; Cabanes et al. 2020; Bardet et al. 2021, 2022), but this is the first time it is applied for an Earth climate study. The present work is thus also an evaluation and validation of the implementation of DYNAMICO in the IPSL earth system model.

To reach the goals described above, we performed a series of forced atmosphere-only simulations following the HighResMIP protocol, with spatial resolutions ranging from 200 to 25 km. We then compared the resulting TCs structures and statistical properties with the robust results of the literature described above, focusing on the global and regional scales but also on the scale of the TCs themselves.

The outline of the paper is as follows. In Sect. 2, we present IBTrACS, our reference database for the observations Sect. 2.1, the IPSL model Sect. 2.2, the simulations Sect. 2.3, the TCs tracking methodology Sect. 2.4, and finally the diagnostics we used Sect. 2.5. The results are presented in Sect. 3 divided into two parts. First, Sect. 3.1 details how resolution affects different aspects of tropical cyclones' climatology. Second, Sect. 3.2 relates some simulated TC properties to their large-scale environment. We summarize our findings and the questions they raise for the future in Sect. 4.

2 Data and methods

2.1 Observations: IBTrACS

In this study, we use data from the International Best Track Archive for Climate Stewardship (IBTrACS, Knapp et al. 2010) version 4 as a reference. It is the most comprehensive database of observed TCs. However, because of its collective

nature, it contains inhomogeneities that must be dealt with, in particular regarding the wind averaging time. In the present paper, we use the “since 1980” subset (Knapp et al. 2018) retrieved on January 8th, 2023. We excluded data before 1980 due to the absence of global satellite coverage before this date, which makes the statistics less reliable. The data processing of the database is the same as in Bourdin et al. (2022), detailed in their Fig. 16. We briefly summarize it below for completeness.

We used data from January 1981 to December 2021 in the Northern Hemisphere (NH), and from July 1980 to June 2021 in the Southern Hemisphere (SH). Tracks labeled as “spur”¹ in the IBTrACS documentation are removed. For consistency with our simulation data, only 6-hourly time steps are kept, and we prefer to use 10-minutes averaged winds. Because of the collective nature of IBTrACS, several wind and pressure values are sometimes provided for a single storm. WMO data are used whenever available. If this is not the case, wind and pressure values are retrieved from other sources as detailed in Bourdin et al. (2022).

Tracks without any wind data or whose maximum wind speed did not reach the tropical storm stage (16 m s^{-1}) are filtered out. Tracks lasting less than one day are also removed. Finally, tracks lacking Sea Level Pressure (SLP) data were kept but not included in those parts of the analysis for which storm intensities are needed, as we prefer to use SLP as a measure of storm intensities (see Sect. 2.5.1 for a discussion of that point).

2.2 The IPSL model

The IPSL-CM model is an earth-system model developed at the IPSL. This paper uses the IPSL-CM6A version of the model that is comprehensively described in Boucher et al. (2020). Since we only consider forced simulations (see Sect. 2.3), we only use the LMDZ6A atmospheric component and the ORCHIDEE land surface component. The physics package of LMDZ6A is described in Hourdin et al. (2020) and the associated documentation is available on ES-DOC. It includes distinct parametrizations for small-scale turbulence, boundary layer convection, deep convection, and cold pools.

As mentioned in the introduction, the present work benefits from the recent developments of DYNAMICO and its implementation in the IPSL-CM6A version of the model in lieu of the original longitude-latitude dynamical core of the LMDZ. Both dynamical cores use a finite difference/finite volume solver, but DYNAMICO (referred to as

“ICO” hereafter) is based on an icosahedral grid. Because its regular grid eliminates the pole singularities of the longitude-latitude grid of the native dynamical core of LMDZ, DYNAMICO’s scalability is improved, and it is now possible to reach higher spatial resolutions when using the IPSL model. The resolution of a given simulation is defined by the number M of subdivisions of a segment of the original icosahedron used to generate the mesh (Dubos et al. 2015). To compare the simulations performed with different values of M (i.e. with different spatial resolutions), we proceed as follows. First, we introduce a length D_i that is the diameter of the circle whose area A_i is the same as that of cell i : $D_i = 2\sqrt{A_i/\pi}$. Next, we define the *effective resolution in the tropics* \mathcal{R} of a grid as the mean of the values D_i for all cells whose latitudes are between 5° and 20° . These boundaries are chosen because this is the latitudinal band where most TC points are found. There are many ways to compute such an effective resolution, but we argue that it is not critical to our work, as it is used only to compare relatively different grids in an given area.

2.3 Simulations

All the simulations were run according to the protocol for Tier 1 historical (1950–2014) atmosphere-only simulations of the HighResMIP framework described in Haarsma et al. (2016). Forcings for solar radiation, ozone, and greenhouse gases concentration are the same as in CMIP6. Specific HighResMIP forcings are a daily $1/4^\circ$ HadISST2-based sea-surface temperatures (SST) dataset and a simplified aerosol optical properties formulation incorporating volcanic and anthropogenic changes.

We used four simulations performed with the IPSL model (see Table 2). Their resolutions are such that $M = 40, 80, 160, \text{ and } 320$. These values correspond to $\mathcal{R} = 202, 101, 51, \text{ and } 25 \text{ km}$ respectively, and the associated simulations are referred to as ICO-LR, ICO-MR, ICO-HR, and ICO-VHR in the following. Small-scale velocity and potential temperature fluctuations are dissipated using Laplacian operators that are iterated twice for the rotational component of the velocity and the potential temperature θ and once for the divergent component of the velocity. The associated dissipation timescales at the smallest scale resolved by the model are noted τ_{rot} , τ_θ and τ_{div} and are used to set the strength of the dissipation operators. In ICO-LR, they are equal to $\tau_{rot} = 21600 \text{ sec}$, $\tau_\theta = 10800 \text{ sec}$ and $\tau_{div} = 3600 \text{ sec}$. They are then divided by two each time resolution is doubled. Although the HighResMIP protocol states that “additional tuning of the high-resolution version of the model should be avoided” (Haarsma et al. 2016), these modifications of the dissipation timescales with spatial resolution were necessary for stability. Similar adjustments are documented for the MPI-ESM HighResMIP simulations for example (Roberts

¹ “spur” tracks are defined as “usually short-lived tracks associated with a main track and often represents alternate positions” in the IBTrACS documentation.

et al. 2020). Therefore, the only differences between these simulations are the spatial resolution in the horizontal direction and the dissipation timescales.

2.4 TC tracking

The choice of the tracking methodology is not innocuous. As shown by several studies (e.g., Horn et al. 2014; Roberts et al. 2020; Bourdin et al. 2022), using a different tracker leads to differences in many aspects of the detected climatology, in particular the frequency and TC days. This is particularly true for weak and short TCs and for the early and late stages of TC tracks. One consequence is that the number and properties of false alarms strongly depend on the tracker. By contrast, strong TCs are detected by all trackers regardless of their algorithm. This analysis provided a good understanding of the relative strengths and weaknesses of the different families of trackers developed by the community.

Based on that work, we chose to use the TempestExtremes framework, and more specifically the TC tracking algorithm from Zarzycki and Ullrich (2017) and Ullrich et al. (2021) (hereafter UZ). This tracker was chosen for the following reasons: (i) It has a very low number of false alarms in reanalyses compared to the other trackers, (ii) it is very quick and convenient to run, which proves particularly handy to analyze the computationally heavy ICO-VHR simulation data, and (iii) this study does not focus on weak tracks.

2.4.1 The UZ tracker

The UZ tracker used here follows the implementation described and tested on ERA5 data by Bourdin et al. (2022). It uses the TempestExtremes framework (Ullrich and Zarzycki 2017) and is essentially identical to the tracker described by Zarzycki and Ullrich (2017). We briefly recall the two steps of the algorithm below for completeness.

1. **Candidate detection** consists in finding all local minima of the SLP and retaining only those points that satisfy the following criteria. SLP must increase by 200 Pa over a distance of 5.5° great-circle-distance (GCD) from the candidate point, and the geopotential thickness $Z_{250-500}$ between 250 and 500 hPa must decrease by 6 m over a distance of 6.5° GCD centered on its minimum value.
2. **Tracks stitching** are obtained by linking together consecutive candidates if they lie within 8° GCD of one another. Tracks must last for at least 54 h (i.e. ten 6-hourly time steps), with a maximum gap of 24 h. Ten 6-hourly time steps (54 h) must also verify the following additional thresholds: $u_{10} \geq 10 \text{ m s}^{-1}$, $|\phi| \leq 50^\circ$, $z_{surf} \leq 150 \text{ m}$, where ϕ and z respectively stand for the latitude and the altitude.

The only difference with the implementation of Bourdin et al. (2022) and Ullrich et al. (2021) is that we used for the present work the geopotential at 250 hPa (instead of 300 hPa) to compute the warm core geopotential thickness, as required by the availability of simulations output data.

Data from January 1951 to December 2014 in the Northern Hemisphere (NH), and from July 1950 to June 2014 in the Southern Hemisphere (SH) are used, unless otherwise stated.

2.4.2 Extra-tropical false alarms filtering

When applied to reanalysis data, TC trackers tend to find many false alarms, i.e., tracks without any observed counterpart. Bourdin et al. (2022) found that many of these false alarms correspond to extratropical cyclones and designed two post-treatment procedures that efficiently filter out those tracks from the catalog of TC tracks obtained from the tracker. Here, we applied their STJ method to the output of the UZ tracker. As for the UZ tracker above, we briefly recall the properties of the STJ filter for completeness.

The STJ filter is based on a 30-day running average of the 250-hPa zonal wind ($\overline{u_{250}}$) and of the horizontal wind speed ($\overline{V_{250}}$). At each time and for each longitude, the sub-tropical jet equatorward limit is defined as the minimum absolute latitude in each hemisphere, for which $\overline{u_{250}} \geq 15 \text{ m s}^{-1}$ and $\overline{V_{250}} \geq 25 \text{ m s}^{-1}$. TC points lying poleward to that limit are labeled extra-tropical (ET). They are removed from TC tracks when computing TC's maximum intensity and position but are retained when computing their lifetime duration. Finally, tracks featuring zero or one non-ET candidate point only are considered extra-tropical cyclones and removed from the analysis. Note that this procedure does not assess the actual structure and nature of the cyclone. It assumes cyclones cannot keep a fully tropical structure poleward of the sub-tropical jet. In ERA5, Bourdin et al. (2022) showed that applying this criterion removes many false alarms but very few actual TCs. In practice, here, the STJ filter removed 0.7%, 5.0%, 12.4%, and 10.7% of the tracks in the ICO-LR, ICO-MR, ICO-HR, and ICO-VHR simulations, respectively. For the ICO-VHR case, this is comparable to the number of tracks removed by the STJ filter in ERA5 (Bourdin et al. 2022).

2.5 Diagnostics

2.5.1 Intensity classification

We used the intensity classification of Klotzbach et al. (2020) based on the minimum SLP and detailed in Table 1. The choice of pressure as a measure for intensity, rather than winds, is made on the grounds of four arguments: (i) there is less uncertainty associated with measures of SLP than winds

Table 1 Tropical Cyclones intensity classification according to Klotzbach et al. (2020), except for the category 0 class, whose threshold (marked as a star) is not in the original classification but has been

Cat	0	1	2	3	4	5
SLP/hPa	1005*	990	975	960	945	925

derived by Bourdin et al. (2022) using the same method. It corresponds to the “tropical storm” category

because of instrumental methods (Klotzbach et al. 2020) (ii) measures of pressure are more consistent across agencies than measure of winds, for which different time scales are used (Knapp et al. 2010), (iii) it provides a more discriminating classification for models, as they have difficulties representing large wind speeds (Knutson et al. 2015; Chavas et al. 2017) but can simulate more of the observed range of SLP, and (iv) SLP is a metric more closely related to TC damage than maximum wind speed (Klotzbach et al. 2020).

Following our filtering procedures for the observations and simulations, we refer to all remaining tracks as TCs throughout the remainder of the manuscript, regardless of their intensities.

2.5.2 TC activity metrics

We used three metrics to quantify different aspects of TC activity.

- TC Frequency (NTC) corresponds to the number of TCs per year.
- TC Days (TCD) is the sum of the duration of each TC per year. All available points of each track (both in the observations and in the simulations) are included in its calculation.
- The Accumulated Cyclonic Energy (ACE) measures the maximum wind kinetic energy. It has units in $\text{m}^2 \text{s}^{-2} \text{yr}^{-1}$ and is calculated according to the relation: $ACE = 10^{-4} \sum u_{10,max}^2$. We aggregate the ACE for all available points of each track in the observations and in the simulations.

Seasonal cycles are computed by binning TCs according to the month they reach their lifetime minimum SLP—excluding ET points.

2.5.3 TC composites

For each TC point, we retrieve snapshots of zonal and meridional winds, vertical pressure velocity, and temperature anomalies using the NodeFileCompose function of TempestExtremes (Ullrich et al. 2021). These fields are then interpolated on a polar grid centered on the SLP minimum. The radial axis goes from 0 to 10°GCD with a 0.2°GCD resolution. The azimuthal axis comprises 16 points evenly spread

between 0 and 360° , hence an angular resolution of 22.5° . The vertical axis coordinate contains seven pressure levels (925, 850, 700, 600, 500, 250, and 50 hPa) for all fields except the vertical velocity, for which the output simulation data only include four levels (925, 850, 500, and 250 hPa). Temperature anomalies are computed as differences with the environmental temperature, which is itself calculated for each snapshot as the averaged temperature of a TC-centered annulus with an inner radius of 1000 km and an outer radius of 2000 km. TC composites are then obtained by averaging the snapshots azimuthally and by pressure category but including only snapshots corresponding to the particular time when a given TC reaches its lifetime minimum SLP.

3 Results

3.1 The impact of the spatial resolution

This section evaluates the sensitivity of TCs climatology in the IPSL model to the spatial resolution. Model results are presented from global to regional to event scales. TCs global activity is discussed in Sect. 3.1.1, regional specificities are detailed in Sect. 3.1.2, then TC-scale properties are quantified in Sect. 3.1.3, including their structure, size and lifecycle. Finally, some of these results are compared with a subset of simulations performed with the native dynamical core of the IPSL model in “Appendix 1”.

3.1.1 Global activity

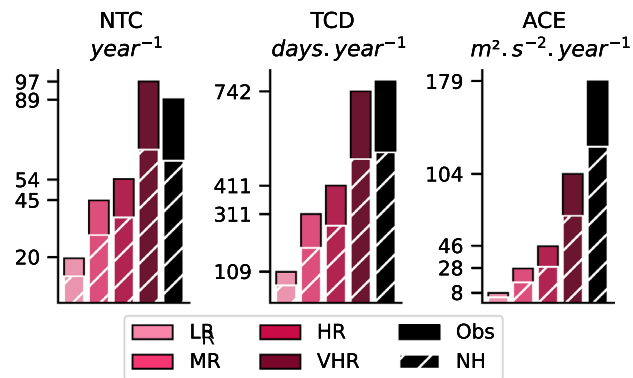
This part evaluates how TC activity evolves at the global scale with horizontal resolution.

Measures of NTC, TCD and ACE for all the simulations are provided in Table 2 and are shown in Fig. 1 for the four simulations and for the observations. The three metrics display a significant increase as the grid is refined. TC frequency and TCD even reach the observed value in the VHR simulation. By contrast, ACE in the VHR simulation only reaches half the observed value. This is because TC maximum wind speeds in the simulations remain well below observed values, a point we will return to below. In agreement with the observations, TC activity is larger in the northern hemisphere for all resolutions, regardless of the metric considered. We also note a slight increase in the

Table 2 TC Activity metrics for the four simulations and the observations

Simulation	Grid	\mathcal{R} (km)	NTC	TCD	ACE
ICO-LR	$M = 40$	202	19.8	108	8.0
ICO-MR	$M = 80$	101	45.7	312	27.8
ICO-HR	$M = 160$	51	55.2	412	45.8
ICO-VHR	$M = 320$	25	98.6	743	104.2
Obs			88	776	179

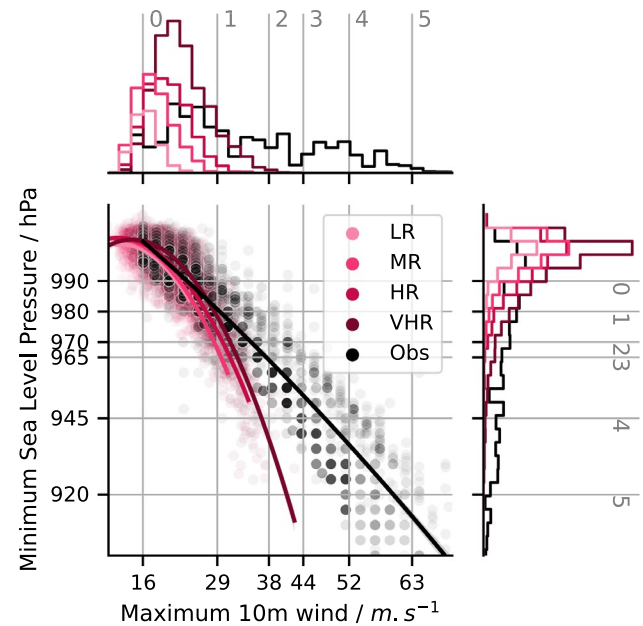
Resolution is quantified using an effective resolution in the tropics defined in Sect. 2.2

**Fig. 1** Frequency (NTC), TC days (TCD), and ACE depending on the resolution, and compared to the observations

proportion of NH TCs with resolution. They account for 60% of the frequency in ICO-LR, compared to 70% in ICO-VHR.

While such an increase in TC activity was expected based on the literature, it does not depend in a simple manner on resolution. There is a large difference between ICO-LR and ICO-MR: TC frequency increases by more than a factor of two, while TCD and ACE triple. By contrast, the difference between ICO-MR and ICO-HR is more modest: it ranges between 20 and 30% for TC frequency and TCD and only amounts to 60% for the ACE. These figures suggest that a plateau might be within reach. However, this does not seem the case: the ICO-VHR simulation significantly increases the three metrics we computed compared to the ICO-HR simulation (+80% in TC frequency and TCD, +128% for the ACE). Based on these findings, we can neither argue that convergence is reached for a horizontal resolution of 25 km nor easily speculate how TC activity would evolve if we doubled the resolution again.

A first step toward a better understanding of these changes with spatial resolution is to characterize the statistical properties of the population of TCs that emerge as the spatial resolution is increased. In agreement with the increase of the ACE, the maximum strength of TCs also increases, regardless of whether it is measured using the maximum 10 m wind speed

**Fig. 2** Central panel: Wind-pressure relationship in the simulations and the observations. A second-order polynomial was fit over the scatter for legibility. Side panel: Marginal distributions of maximum wind speed and minimum SLP, shown as unnormalized (raw counts) histograms

or the minimum SLP (see side panels in Fig. 2). Intensity increases more in terms of SLP than it does in terms of winds. Typically, pressure category 3 is reached in ICO-HR and 4 in ICO-VHR, whereas only wind categories 1 and 2 are reached in ICO-HR and ICO-VHR, respectively. As reported several times in the literature (Roberts et al. 2015, 2020), this difference also manifests itself in the scatter plot shown in Fig. 2 that reports minimum sea-level pressures against maximum 10 m wind speeds for each track in the simulations and the observations. The simulated wind-pressure relationships remain below the observations for all spatial resolutions, with a more pronounced disagreement in the maximum wind speeds than in the minimum SLP. This is investigated further by discussing outer size in Sect. 3.1.3. On the other side of the intensity distribution, we find a systematic increase in the number of weak storms, with typical wind speeds of order 20 m s^{-1} and minimum SLP larger than 990 hPa (Fig. 2), and relatively short-lived storms, with duration smaller than 5 days (Fig. 3). In ICO-VHR, the deficit in strong TCs is thus balanced by an excess of weak and short tropical storms. It remains difficult to disentangle whether this population corresponds to precursors that existed at lower resolution simulation but were not intense enough to be detected or to a new population of storms that appeared in ICO-VHR. Likewise, we do not know whether these weak and short TCs will intensify for finer spatial resolutions such that the intensity and duration distributions will

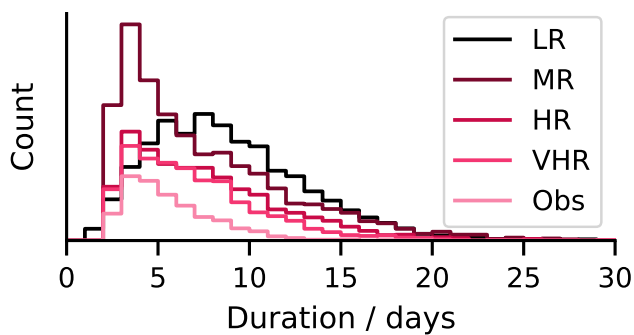


Fig. 3 Count histogram of the TC duration in each simulation and the observations

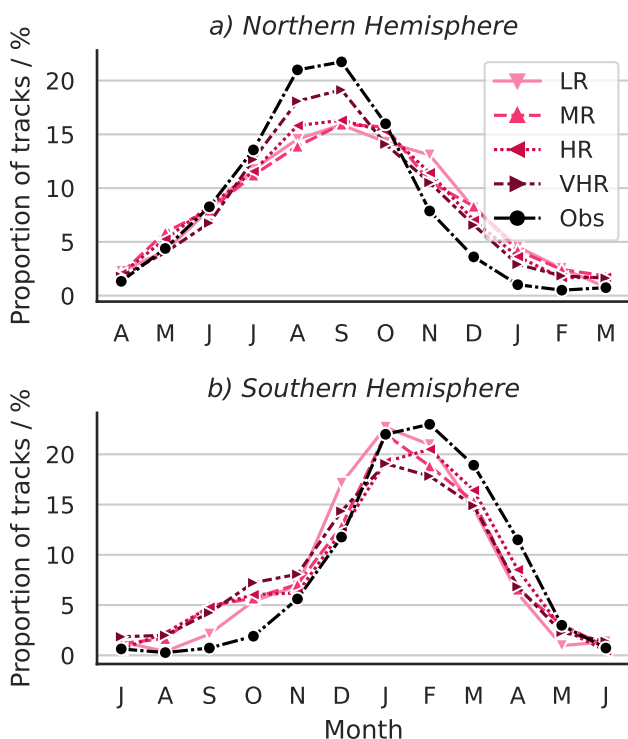


Fig. 4 Seasonal cycle in the Northern (top) and Southern (bottom) hemisphere, depending on the resolution and compared to the observations. TCs are binned according to the month during which they reach their lifetime maximum intensity, as measured in terms of minimum SLP and excluding ET points

converge to the observed distributions or whether additional TC seeds will keep appearing as resolution increases.

Finally, the hemispherically averaged seasonal cycles of TC activity are plotted in Fig. 4 for simulations and observations. They are nearly identical in all the simulations and very close to the observations, displaying a peak in each hemisphere's late summer/early autumn. In the northern hemisphere (Fig. 4a), the TC season is slightly too long, with a tendency to last longer than observed. This latter bias tends

to decrease with increasing resolution. By contrast, the TC season occurs too early in the southern hemisphere (Fig. 4b), and that bias tends to accentuate with increasing resolution. In the following subsection, we will return to some regional specificities of the seasonal cycle.

3.1.2 Regional activity

While global statistics inform us about the overall ability of our model to generate tropical cyclones, it is important to look specifically at individual basins because tropical cyclogenesis characteristics and processes are not the same everywhere. This part evaluates whether our simulations meet the expectation that the geographical repartition and properties (duration, intensities and seasonal cycles) of TCs improve with increasing resolution. The basin definition and nomenclature we used correspond to WMO standard.

Fig. 5 plots NTC, TCD and ACE decomposed by oceanic basins for the different simulations and in the observations. In the observations, the WNP is the most active basin regardless of the metric. TC frequency is almost twice as large as that of the NATL and ENP basins, which have similar activity levels. The three southern hemisphere basins display lower frequencies, with the SI being more active than the AUS and the SP being the least active. Finally, the NI and the CP are the last two basins, with the NI featuring a few weak TCs per year, while the CP has even fewer but more intense TCs than the NI.

The ICO-LR simulation fails to capture the observed geographical pattern of activity. TC frequencies are smaller than 5 TCs per year in all basins. For most cases, this is much smaller than the observed frequencies. Activities in the NATL and SP basins are even strikingly low ($\sim 1 \text{ yr}^{-1}$). The only exception is the NI, which stands out as an outlier in the sense that the simulated frequency (4 yr^{-1}) almost matches that observed (5 yr^{-1}).

ICO-MR and ICO-HR are very similar in terms of their regional TC activity, as they are in terms of their global TC activity. The regional distribution of TC frequency, TCD, and ACE are similar. The ENP is the most active basin, followed by the NI, the SI, and the AUS basins. TC frequency in the ENP and the SI are comparable to the observations, while it is overestimated by almost a factor of two in the NI. For these two resolutions, the WNP and NATL basins still stand out as being too quiet. They are respectively ranked 5th and 6th in terms of NTC in ICO-MR and ICO-HR, instead of 1st and 3rd as observed. TC activity in the SP and CP remains elusive. In ICO-MR and ICO-HR, we thus see that individual basins start to distinguish themselves. However, the model still fails at reproducing the observed levels of TC activity in some of the most active basins.

In ICO-VHR, the WNP and ENP basins are the most active and display similar TC frequencies, although ACE

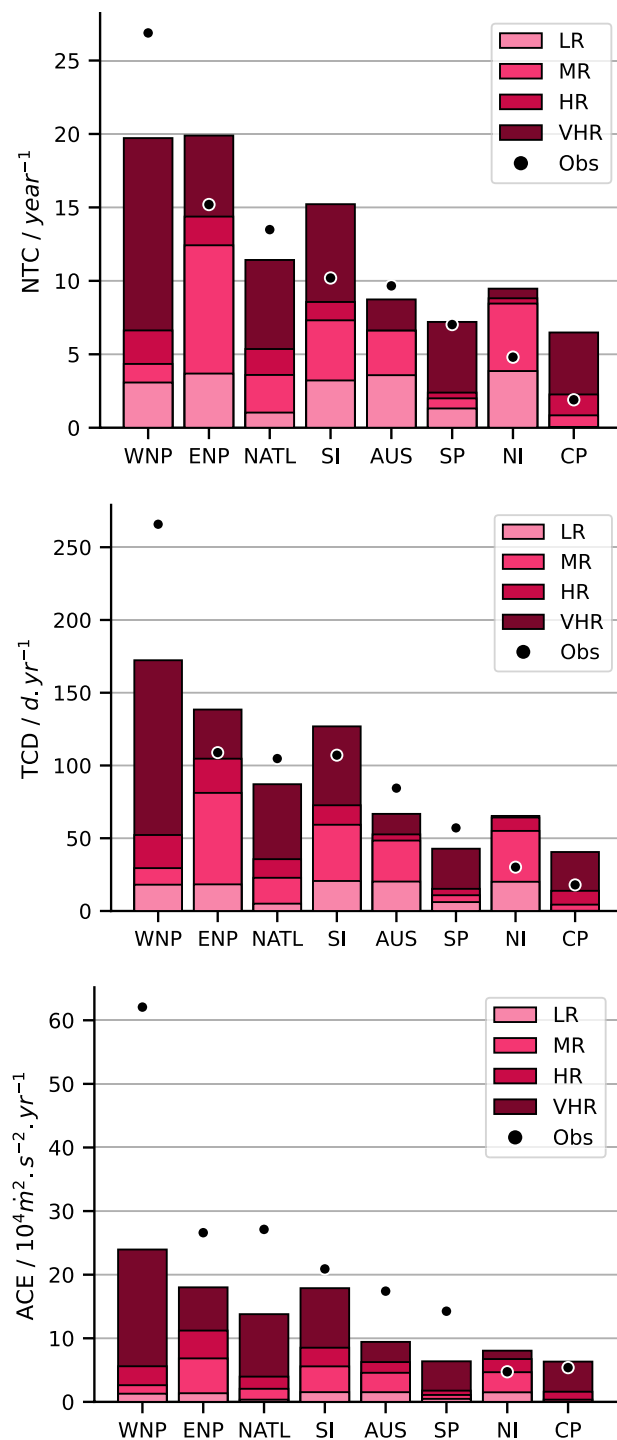


Fig. 5 Basin NTC (top panel), TCD (middle panel) and ACE (bottom panel) in each simulation compared to the observation. Basins are displayed in order of decreasing frequencies in the observations

in the WNP is 33% larger than that of the ENP. We note, however, that TC frequency in the WNP is still underestimated in ICO-VHR compared to the observations. When ranking the other individual basins according to their TC

frequency, we find, in the following order, the SI, NATL, NI, AUS, SP, and CP basins. This is close to the observed ranking (see Fig. 5).

In conclusion, we find a clear improvement of the inter-basin geographical distribution of TC activity as spatial resolution is increased. The ranking of the basins in terms of TC frequency in ICO-VHR is similar to the observed one, even if the pattern shows less contrast between the different basins than observed. This is essentially because the most active basin (WNP) displays a negative activity bias, while simultaneously, the least active basins in the observations (NI and CP) are too active in the simulations. The SI also shows comparatively too much activity. The intra-basin properties and geographical distribution of TCs also improve with spatial resolution. This is discussed in detail in “Appendix 2”, and we briefly summarize the main points here:

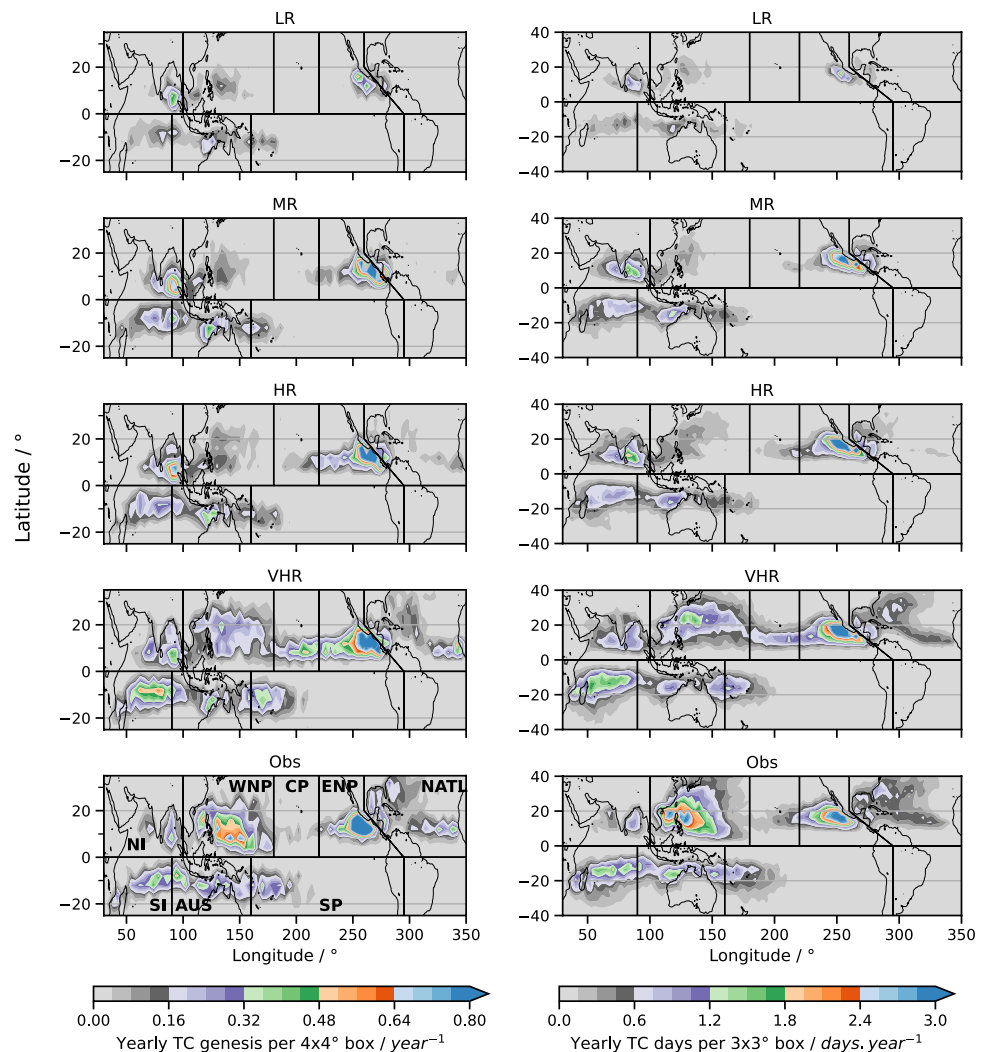
- TCs genesis and track density tend to approach the observed spatial distribution as resolution is increased (Fig. 6). There are few exceptions, though. In the WNP, there is a northward shift of both patterns compared to the observations which becomes obvious in ICO-VHR. There is also an excess of TCs near the coast of Guatemala in the ENP. By contrast, TCs in the NATL are well simulated, and particularly so in ICO-VHR. We will come back to a more detailed analysis of the WNP and NATL basins in Sects. 3.2.3 and 3.2.4, respectively.
- In general, there is an excess of short (Fig. 16) and weak (Figs. 17 and 18) tracks in all basins.
- TCs seasonal cycles are well captured in all basins (Fig. 19), except in the SI where there is an excess of TCs earlier than observed (by about two months) and a deficit of TCs during the observed cyclonic season. In the peculiar NI, the two peaks of TC activity are simulated, although with a smaller maximum than observed in spring.

It is interesting to note that there are some similarities between these results and the outcome of other models that followed the HighResMIP protocol, such as described by Roberts et al. (2020). All six high-resolution models discussed in that paper display a deficit in the WNP or at least in the South China Sea. In the ENP, the pattern we find of having too many TCs near the coast of Guatemala is also present in several models.

3.1.3 TC properties

We now describe the impact of spatial resolution on TC-scale properties, namely their structure and lifecycle.

Fig. 6 Genesis (left) and track (right) density for each simulation and in the observations. Limits of the basins according to the WMO standard are overlaid



3.1.4 TCs structure

Figure 7 displays composites of the circulation and the temperature distribution for TCs of category one and above in each simulation. Quantitative measures calculated from these composites are shown in Fig. 8.

For all TC categories and all resolutions, the composites display the expected features typical of TCs. We observe a distinct warm core in the upper troposphere, between 500 and 250 hPa (Fig. 7b), cyclonic rotation around the TC center, as shown by the tangential winds that peak in the lower troposphere and decrease both upward and outward (Fig. 7a), and a secondary circulation composed of lower level convergence and upper-level divergence (Fig. 7a), associated with rising motions in the central region of the TC (Fig. 7b).

The primary and secondary circulations and the warm core anomaly increase in strength with the TC category. The warm core temperature anomalies increase from values of about 6.7 K for category 1 TCs, to 8.5 K for category 2, to

about 10 K for category 3, and reach 13 K for the strongest storms (Figs. 7b and 8h). This increase in temperature anomaly with intensity is documented in the observational study of Wang and Jiang (2019), who found warm core temperature anomalies reaching 8, 11, 12, 13, and 15 K in composites of TCs in categories 1 to 5, respectively. Our model simulates comparable values, although slightly underestimated.

Likewise, tangential winds increase from about 22 m s⁻¹ for category 1 TCs up to 38 m s⁻¹ for category 4 (Figs. 7a and 8a). However, as already noted above, they never reach the observed levels of the strongest storms. Radial and vertical winds associated with the secondary circulation also increase in amplitude for increasing TC categories. Upward motion (Fig. 8e) remains, however, well below the expected order of magnitude of 5 to 10 m s⁻¹ (Emanuel 2003). Although we do not find any downdraft near TC centers that would be a signature of the existence of a TC eye, a noteworthy feature of the secondary circulation is that the rising motions systematically reach their maximum

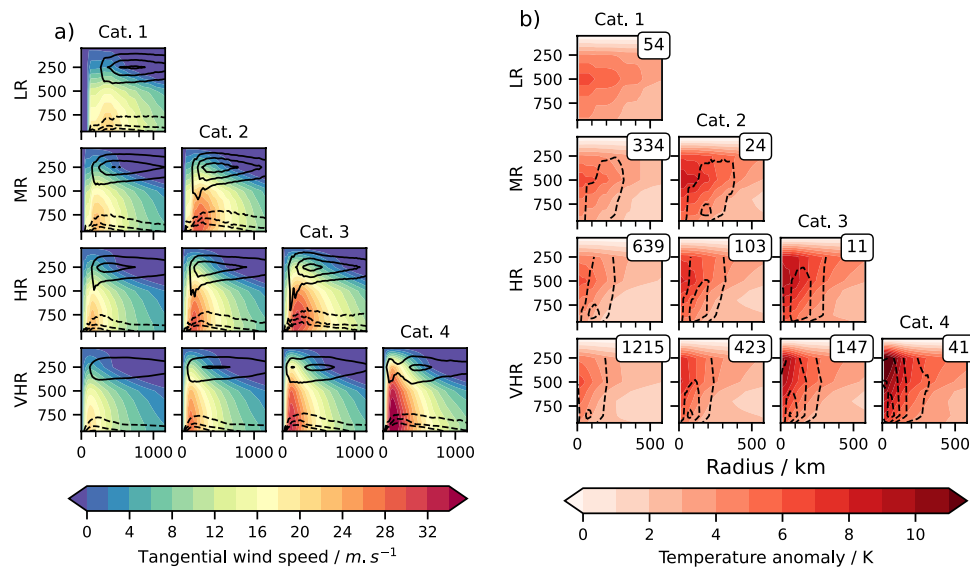


Fig. 7 Composites of azimuthally-averaged TC structure, depending on the resolution and the storm pressure category. In each subplot, the x-axis is the radius in km, and the y-axis is the pressure in hPa. Composites include only the snapshot that corresponds to the particular time at which a given TC reaches its lifetime minimum SLP (i.e. there is only one used snapshot per track). The number of snapshots for each composites is indicated in a white box in panel **b**), and is identical for the panel **a**). **a**) Shading represents azimuthal wind speed, and contours represent the radial wind speeds. Radial velocity contours

are drawn every m/s, except 0 m/s. Dashed contours correspond to negative radial velocities (inwards). **b**) Shading represents temperature anomaly, and contours represent the pressure velocity. Pressure velocity contours are drawn every 0.3 Pa/s between -1.2 and -0.3 Pa/s. Temperature anomalies are computed as differences with the environmental temperature, which is defined as the averaged temperature within a TC-centered annulus of inner radius 1000 km and outer radius 2000 km

value off the center, even at low resolution (Fig. 7b). This is in qualitative agreement with the observations and in contradiction with most models in Moon et al. (2020), where maximum rising motion is often found at the center of modeled TCs, particularly at low resolution.

In agreement with Moon et al. (2020), we find that tangential wind amplitudes and warm core anomalies are not sensitive to the spatial resolution for a given TC category (Fig. 8a, h). However, this is not true for many other aspects of TC's 3D structures. First, there is a systematic tightening of both the primary and secondary circulations with increasing resolutions. For example, the radius of maximum tangential wind (RMW) decreases from about 3° (i.e., ~ 300 km) at LR to 2° (~ 200 km), 1.5° (~ 150 km) and 1° (~ 100 km) at MR, HR, and VHR, respectively (Fig. 8b). Such a decrease of the RMW with resolution echoes a similar finding by Manganello et al. (2012). We note, however, that these authors report smaller values of the RMW. For example, at a resolution of 39 km that is intermediate between our HR and VHR, they found an RMW equal to 0.75° , or about 75 km. By contrast, our measurements at VHR agree with the RMW of TCs in ERA5, whose resolution is similar and for which Dulac et al. (2023) recently reported a value of about 100 km. In any case, these values remain larger than the typical observed values of 20 to 50 km for the RMW (Emanuel 2003). This is simply because our resolution is

still too coarse to describe inner TC flow structures properly. Finally, the RMW increases (resp. is constant) with TCs categories for ICO-LR, ICO-MR (resp. ICO-VHR), in apparent conflict with the observations that RMW decreases with TC strength (Mallen et al. 2005). The reason for that discrepancy is unclear and requires further investigation.

The secondary circulation also features a significant sensitivity to resolution. For all TC categories, radial inflow and outflow wind speeds systematically decrease with increasing resolution (Fig. 8c, d). By contrast, the vertical velocity u_{vert} increases (Fig. 8e). This might appear paradoxical at first glance. However, the radius r_{max} at which the vertical velocities (Fig. 8f) reach their maximum decreases with resolution in such a way that $u_{vert} \times \pi r_{max}^2$ is generally smaller at finer resolution (Fig. 8g). For example, for category 1 TCs, $u_{vert} \times \pi r_{max}^2$ is almost twice as large in ICO-MR compared to ICO-VHR, and for category 2 TCs, $u_{vert} r_{max}^2$ is 60% higher in ICO-MR compared to ICO-VHR. This shows that the upward mass flux decreases with resolution. Overall, we thus conclude that the secondary circulation weakens for a given TC category as resolution increases. More analysis is required to understand better that sensitivity, but it may be because the amount of heat required to produce the warm core temperature anomalies decreases with resolution because the volume of the core region decreases due to the tightening of the TC structure described above.

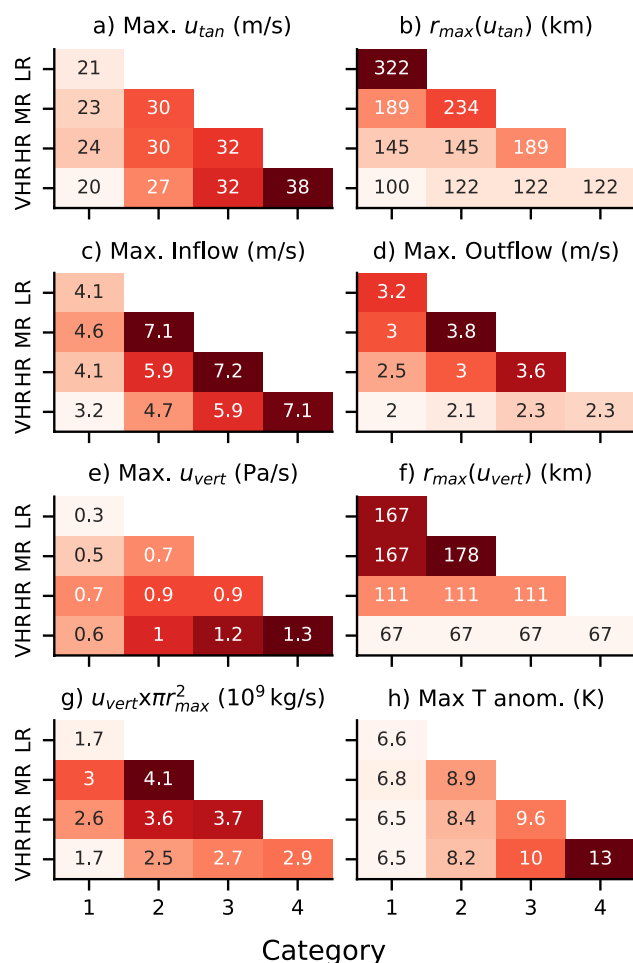


Fig. 8 Measures relative to each composite in Fig. 7. **a)** Maximum tangential wind speed in m/s; **b)** Radius of maximum tangential wind in °GCD; **c)** Maximum inwards velocity (Minimum of radial wind speed) in m/s; **d)** Maximum outwards velocity (Maximum of radial wind speed) in m/s; **e)** Maximum pressure velocity in Pa/s; **f)** radius of maximum pressure velocity in °GCD; **g)** Upward mass flux defined as the product of the maximum pressure velocity and surface of the circle whose radius is the radius of maximum pressure velocity; **h)** Maximum temperature anomaly in K

One of the main findings is thus that the size of TC inner structures (as measured by the radius of maximum tangential wind or by the radius of maximum vertical velocity) decreases with increasing resolution. We expect, however, that their outer structure, on scales of order 500 to 2000 km, is less sensitive to resolution. Such spatial scales are indeed about one order of magnitude larger than the grid size, even for the ICO-LR simulation, for which $\mathcal{R} = 202$ km. To examine that point, figure 9 shows the profile of the surface tangential wind against \tilde{r} , which corresponds to the radius r normalized by the deformation radius R_d . The latter is defined according to

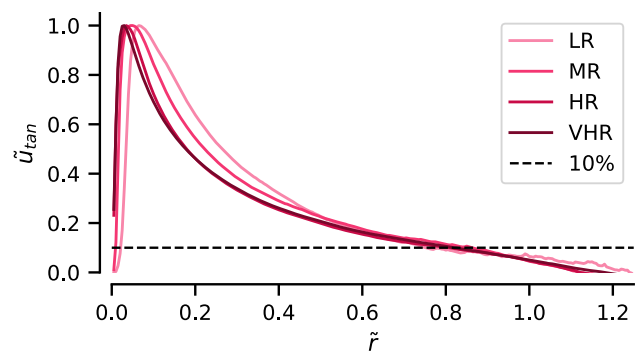


Fig. 9 Normalized composite profiles of tangential wind against the dimensionless radius \tilde{r} for each resolution

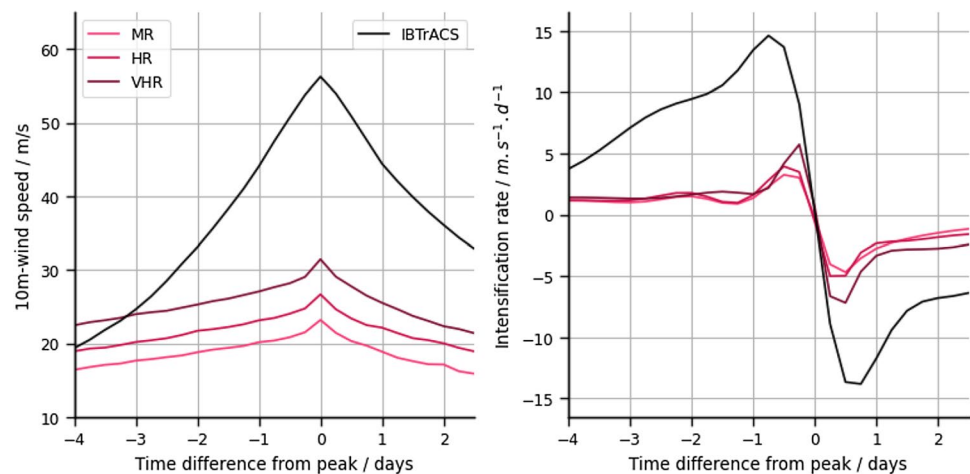
$$R_d = \frac{NH}{f_0}, \quad (1)$$

where N is the Brunt–Väisälä frequency, H is the tropopause height, and f_0 is the Coriolis parameter at the cyclone's center. For all resolutions and all TCs, we found that N and H are almost constant and equal to $7.6 \times 10^{-3} \text{ s}^{-1}$ and 15 km, respectively. By contrast, f_0 varies by a factor of three for latitudes ranging from 10° to 30° , a signature of the Coriolis force increasing with latitudes. The increase in Coriolis parameter impacts TCs outer structure, which is accounted for by normalizing the radius by R_d . In agreement with our expectations, the normalized tangential wind profiles converge to a single profile, independent of the spatial resolution, in TCs outer parts ($\tilde{r} \gtrsim 0.5$), while differing in the inner parts ($\tilde{r} \lesssim 0.4$), as detailed above (Fig. 9). We can thus define a radius $r_{10\%}$ at which the 850 hPa tangential wind amounts to 10% of its maximum value. We find $r_{10\%} \sim 0.8R_d$ regardless of the spatial resolution.

3.1.5 TCs lifecycles

Figure 10 (left panel) shows the mean lifecycle of the 10% most intense TCs in each simulation (except ICO-LR, for which there are not enough intense tracks) compared to the observations (black line). The shapes of the simulated TC lifecycles are very similar in the three simulations. During TCs intensification, there is a steady linear increase in wind speed up to 6 h before the peak. At this point, there is a sharp increase up to the maximum wind. After reaching the peak, the wind decreases with a slightly steeper slope than during intensification. On the right panel, the intensification rate stagnates around $1.2 \text{ m s}^{-1} \text{ d}^{-1}$ until one day before the peak, regardless of the spatial resolution. Intensification rate during the day preceding the peak increases with spatial resolution. The maximum intensification rate is attained at the last time step before the peak and reaches $3.2 \text{ m s}^{-1} \text{ d}^{-1}$ in the ICO-MR simulation, $4.0 \text{ m s}^{-1} \text{ d}^{-1}$ in ICO-HR and

Fig. 10 Left panel: Mean lifecycle of the 10% most intense TCs in each dataset. Right panel: Intensification rate corresponding to the mean lifecycle for each dataset. Intensification rates are obtained by taking the first-order derivative of a spline interpolation of the mean lifecycle



$5.9 \text{ m s}^{-1} \text{ d}^{-1}$ in ICO-VHR. The dissipation rate is maximum about 12 h after the peak, and reaches $-4.6 \text{ m s}^{-1} \text{ d}^{-1}$ in the ICO-MR and ICO-HR simulations and $-7.0 \text{ m s}^{-1} \text{ d}^{-1}$ in ICO-VHR.

The observed lifecycle is quite different. The intensification stage is exponential, with a maximum intensification rate of $15.9 \text{ m s}^{-1} \text{ d}^{-1}$. The dissipation stage, however, presents a proportionally similar behavior, with a maximum dissipation rate of $-13.5 \text{ m s}^{-1} \text{ d}^{-1}$. This observed dissipation rate is thus twice as large as the simulated dissipation rate measured in ICO-VHR, for which the winds are two times smaller.

The origin of these differences is not clear and deserves further investigation. Similar results were found when analyzing the lifecycle in terms of SLP instead of wind speed (not shown). However, they agree with the simulations of Manganello et al. (2012), who also described lower intensification rates in their simulations than in the observations. In reanalyses, Dulac et al. (2023) also highlighted that ERA5 had a sharper peak around the maximum wind than the observations, which is also the case in our simulations.

3.2 TC and large-scale environment

We now turn to an analysis of the relationship between the simulated large-scale environment and TC activity (NTC and ACE). An ensemble of simulations would be preferable to assess that aspect. However, it is too expensive to obtain at high resolution. In addition, we are limited in the comparison we can make to the period (1981–2014) during which observations and simulations overlap, namely 34 years. This is still longer than previous studies that performed the same analysis (Manganello et al. 2012; Strachan et al. 2013). In the two first subsections, we investigate how the simulated interannual variability in the model correlates with the observations and El

Nino-Southern Oscillation (ENSO, Trenberth 2020). Then, we focus on two basins in the ICO-VHR simulation: The WNP, where the VHR model still displays a significant TC deficit, and the NATL, where the climatology of TCs is very good.

3.2.1 Interannual variability

The simulations we analyze in the present paper are “historical,” meaning that the various forcings (SST, greenhouse gases, and aerosols) equal the observed values over the 1950–2014 period. Therefore, we expect the model to reproduce some of the observed interannual variability of TC activity. This skill is important considering the fact that climate models are at the heart of TC dynamical seasonal forecasts (Befort et al. 2022; Camargo and Wing 2016).

We thus start by computing the correlations between the observed and simulated yearly TC activity. Table 3 shows the Pearson correlation coefficients between the observations and the simulations for the yearly NTC over the period

Table 3 Pearson correlation coefficient for the yearly number of TC in each basin compared to the observation

	LR	MR	HR	VHR
Global	0.31	0.01	-0.05	0.32
WNP	0.26	0.17	0.31	<i>0.48*</i>
ENP	<i>0.43*</i>	0.36**	0.37**	0.47**
NATL	0.16	0.54**	0.36**	0.51**
NI	-0.11	0.19	0.02	0.20
SI	-0.11	0.13	-0.07	0.09
SP	0.17	<i>0.35*</i>	-0.34	<i>0.41*</i>
AUS	0.07	0.19	0.19	<i>0.39*</i>
CP	0.21	0.20	0.31	<i>0.57*</i>

* and italic denotes significant correlations (p -value ≤ 0.05). ** and bold denotes basins and resolution for which a significant correlation (p -value ≤ 0.05) was also found for ACE (see Online Appendix Table C2)

1981–2014. In Online Appendix C, we also show the same Pearson correlation coefficients for the ACE (Online Appendix Table C2) and the Spearman correlation coefficients for NTC and ACE (Online Appendix Tables C3 and C4). Correlations are considered statistically significant when the associated p -values is below 0.05, i.e. when there is a probability smaller than 5% that observed and simulated TC frequencies are uncorrelated. Cases displaying statistically significant Pearson correlations for both the NTC and the ACE appear in bold in Table 3.

First, no statistically significant correlation exists between the observed and simulated NTC at the global scale for all resolutions. This result also holds when using Spearman's correlation (Online Appendix Table C4). There are, however, statistically significant correlations in individual basins between the simulated and observed TC activities. In addition, the number of basins with a significantly correlated NTC tends to increase with spatial resolution. Indeed, one, three, two, and six oceanic basins display statistically significant correlations in ICO-LR, ICO-MR, ICO-HR, and ICO-VHR, respectively. In the ICO-VHR simulation, all basins except the North and South Indian Ocean show a statistically significant correlation for the NTC, although we note that this is not the case for the ACE. The simulated ENP TC frequency is the only one significantly correlated with observations at all resolutions. In the NATL, statistically significant correlations are found for resolutions MR and above. For both basins, there is also a statistically significant Pearson and Spearman correlation between the observed and simulated ACEs for resolutions MR and above (see Online Appendix Tables C2 and C3). It must be noted, however, that even the statistically significant correlations remain rather weak: The correlation coefficients indeed rarely exceed a value of 0.5.

These findings echo some results already published in the literature. For example, Manganello et al. (2012) also found strong correlations between their simulated TC activity and the observations for all northern hemisphere basins (except for the North Indian) over the period 1990–2008 (i.e., 18 years). Likewise, Strachan et al. (2013) report significant correlations in the NATL at all resolutions and in the ENP at high resolution but failed to observe any in the other basins, including the WNP over the period 1980–2000 with 3 ensemble members. This is similar to the correlations we obtained in our ICO-HR simulation, the spatial resolution of which is the closest to their best spatial resolution, which is of order 60 km.

3.2.2 Link with ENSO

We next investigate whether TCs frequencies in our simulations correlate with ENSO on a yearly basis. There is ample observational evidence that this is indeed the case in the

Table 4 Pearson correlations coefficient between the yearly ACE or NTC and the mean of the ONI index between August to October of the same year

Variable	Data	WNP	ENP	NATL
ACE	Obs	0.68*	0.40*	− 0.48*
	ICO-VHR	0.08	0.39*	− 0.44*
NTC	Obs	− 0.07	0.46*	− 0.55*
	ICO-VHR	− 0.05	0.04	− 0.59*

* and bold denote significant correlations ($p < 0.05$)

North Pacific and North Atlantic basins (Camargo et al. 2010), and it is an important target of models in general to reproduce such a relationship. ENSO is a phenomenon arising from the ocean and atmosphere coupling. In our simulations, SSTs are imposed, so there is no atmospheric feedback onto the ocean. However, the SSTs we prescribe are observed SSTs, meaning they already embed the observed oceanic part of ENSO. We checked that the atmosphere is reacting as expected to the imposed SSTs from 1959 to 2014. The Southern Oscillation Index (SOI, Ropelewski and Jones 1987), a measure of the SLP gradient between Tahiti and Darwin, is very close in the simulations to the observed SOI (not shown). The mean zonal wind in the 5°N–5°S/170°W–120°W also correlates very well with the observed mean zonal wind (not shown). We conclude that the simulations accurately capture the link between ENSO and the atmospheric circulation.

To go further in the analysis, Table 4 shows the correlations between the yearly ACE and NTC and the mean Oceanic Niño Index (ONI) averaged over August to October of that same year. In the North Atlantic, La Niña years correspond to enhanced observed TC activity. It means the observed ACE and NTC should negatively correlate to the observed ONI. As shown in Table 4, this is indeed the case for both measures of TC activity. In addition, these negative and statistically significant correlation coefficients are also found in the simulation ICO-VHR with values that are remarkably close to the observed correlation coefficients. The results we obtained for the Eastern North Pacific are more mixed. There are statistically significant correlations between the observations and the ICO-VHR simulation between the yearly ACE and the ONI. However, the model does not reproduce the observed correlation between the NTC and the ONI. We finally turned to the Western North Pacific, for which a significant correlation exists in the observations between the ACE and the ONI but not between the NTC and the ONI. The ICO-VHR simulation fails to capture these properties. There is simply no correlation between any of these variables and the ONI.

It is interesting to compare these findings with the results of Manganello et al. (2012) who performed a similar

analysis.² First, Manganello et al. (2012) report observed correlations with ENSO that are similar to the values we find for all three basins. Like us, they also find a statistically significant correlation in the ENP in their model. However, in sharp contrast with our results, their simulations are able to capture the observed correlation in the WNP, but fails to do so in the NATL. These differences are not surprising. We already noted large biases of TC activity in the WNP and a comparatively better TC climatology in the NATL. In the following two sections, we will focus on these two basins and try to understand these differences better.

3.2.3 Western North Pacific

As discussed above, there are several shortcomings of the WNP TC activity climatology: the frequency of TCs is too low compared to the observations and their geographical distribution is biased northward. It also extends too far east, and the simulated interannual variability of the ACE is neither correlated with the observations nor with ENSO. In this part, we test the hypothesis that this deficit is associated with large-scale biases in the model.

Early on, studies based on observations identified variables defining a large-scale environment favorable to tropical cyclogenesis (Gray 1975; McBride and Zehr 1981). These variables were combined into Genesis Potential Indices (GPIs), which are often used in the literature as dimensionless indicators of large-scale conditions favorable for TC genesis (Gray 1979; Tippett et al. 2011; Royer et al. 1998; Emanuel 2004). They are generally computed from the product of dynamical and thermal components. Although the precise formulas vary among authors, most GPIs consider the following variables or some equivalent of these variables: absolute or relative vorticity and vertical wind shear for the dynamical part; SST or Potential Intensity (PI) and relative humidity or moist entropy deficit for the thermal part (Cattiaux et al. 2020; Camargo and Wing 2016). In the following, we use the GPI introduced by Emanuel (2004) and defined according to the following relation:

$$\text{GPI} = \beta \times \frac{|10^5 \eta_{850}|^{3/2}}{(1 + 0.1 V_{\text{shear}})^2} \times \left(\frac{H_{600}}{50} \right)^3 \left(\frac{V_{\text{pot}}}{70} \right)^3,$$

where β is a scaling factor, basin-dependent. Here, we choose β so that the ratio of the frequency in a basin to the integral of the GPI over the same basin is the same in ERA5 and ICO-VHR.

² It should be noted that Manganello et al. (2012) use the Power Dissipation Index (PDI) instead of the ACE. The PDI and the ACE are similar quantities that are both sensitive to the strongest TCs. To validate our findings, we made sure the results shown in Table 4 are qualitatively similar regardless of whether we use the PDI or the ACE (not shown).

In the following, we focus on the spatial variations of the four fields used to compute the GPI, because they are deemed the most important large-scale variables influencing TC genesis.

- Absolute Vorticity at 850 hPa, $\eta_{850} = \zeta_{850} + f$, in s^{-1} ;
- Vertical wind shear between 850 and 200 hPa, V_{shear} , in $m s^{-1}$;
- Relative Humidity at 600 hPa, H_{600} in %;
- Potential Intensity (PI), noted V_{pot} and which is a function of SST, the vertical profiles of pressure, temperature, and humidity, in $m s^{-1}$.

The formulation of the GPI means that a favorable environment conducive to TC formation is humid air, warm sea surface temperatures, a weak vertical shear and large cyclonic vorticity. In the following, ERA5 is considered the observational reference for those large-scale fields, assuming it accurately represents the WNP climate (Li et al. 2021).

Figure 11 shows WNP zooms of TCs track density, genesis density, and climatological GPI in IBTrACS/ERA5 (first column) and ICO-VHR (second column). The GPI is computed using the relevant large-scale variables averaged over the July to October (JASO) period. The rightmost column represents the associated biases computed as differences between the simulation and the observations or ERA5.

As already discussed in Sect. 3.1, there is a deficit in TC frequency and TCD in the WNP and an excess in the CP (Fig. 12, first row). The WNP deficit is not uniform but takes the form of a dipole: a large negative bias, up to -2 TC days per year per $3 \times 3^\circ$ box East of the Philippines, and a smaller excess ($+0.5$ TC days per year per $3 \times 3^\circ$ box) in the north-eastern part of the basin. The negative bias is associated with a negative bias of TCs genesis density in the southern WNP. Half of the positive bias is due to an excess of TCs forming in the CP (Fig. 11, second row) that travel to the WNP after their formation (not shown). Interestingly, this WNP northward shift of TCs genesis density resembles a similar northward shift of the maximum location of the GPI (Fig. 11, third row). Indeed, in the southern part of the WNP, the negative biases of the GPI and the TCs genesis density have similar shapes (Fig. 11, bottom left panel). This suggests that the northward shift of TCs genesis density is due to one or more of the environmental variables entering the GPI.

To further investigate this potential link, their climatological distributions in ERA5 and ICO-VHR and the associated biases of the ICO-VHR simulation with respect to ERA5 during the TC season are shown in Fig. 12. The relative humidity has a maximum in the simulation located too far north compared to the reanalysis. Consequently, the warm pool, one of the most humid areas of the globe, is too dry in the simulation, with only about half of the

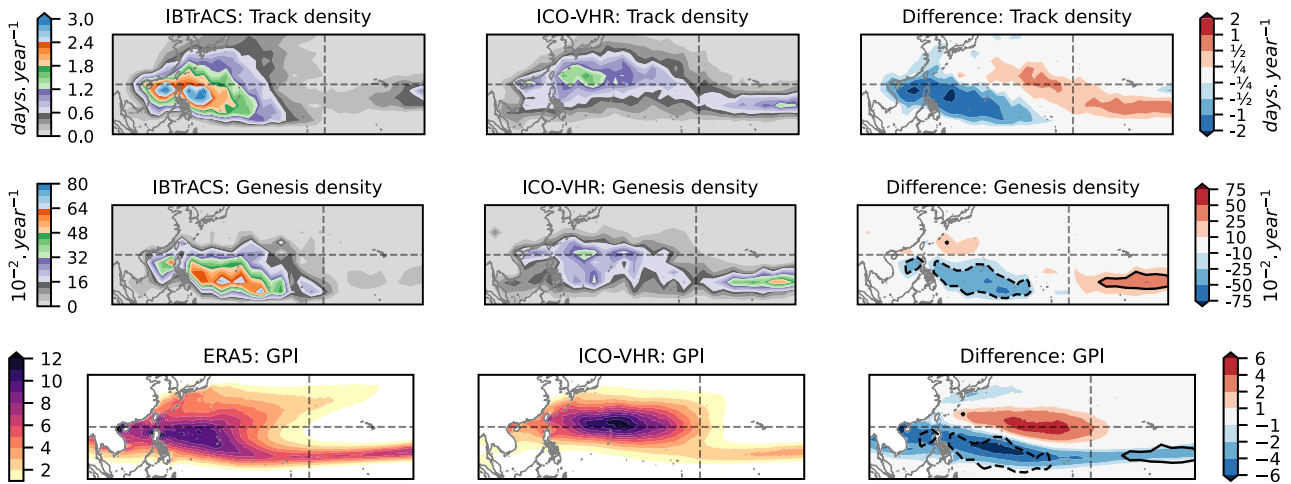


Fig. 11 Comparison of track density, genesis density, and GPI in ICO-VHR and reference (IBTrACS for tracks and ERA5 for GPI). The dateline (180°) and the 20°N parallel are displayed as dashed lines. The black contours represent the -0.5 and $+0.5 \text{ year}^{-1}$ ICO-

VHR genesis density bias (middle and bottom right panels). GPI is displayed as the climatological mean between July and October (included). Track density is computed over 3×3 deg boxes, and genesis density over 4×4 deg boxes

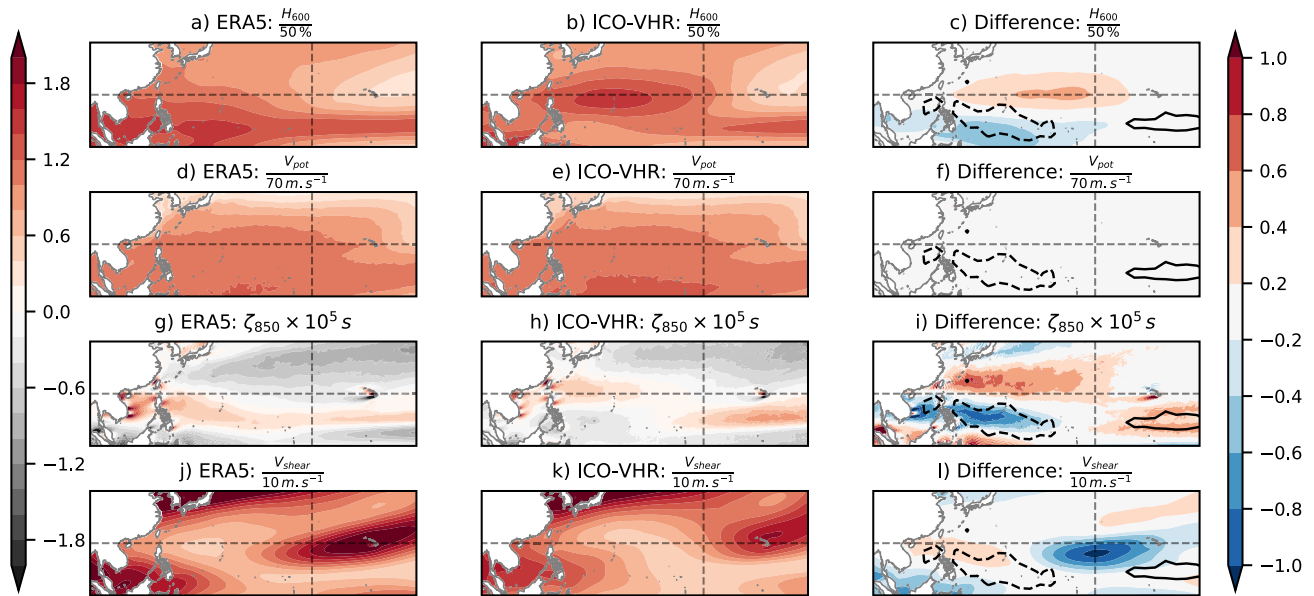


Fig. 12 Comparison of environmental variables in ERA5 (left column) and ICO-VHR (middle column): 500 hPa relative humidity (first row), Potential Intensity (second row), 850 hPa relative vorticity (third row), vertical wind shear (fourth row). The dateline (180°)

and the 20°N parallel are displayed as dashed lines. The black contours represent the -0.5 and $+0.5 \text{ year}^{-1}$ ICO-VHR genesis density bias (right column). Fields are displayed as the climatological mean between July and October (included)

relative humidity of ERA5. There is also a large deficit of relative vorticity in the western WNP between 5 and 20°N, representing 100% of ERA5 climatological value. It is associated with a bias in the lower troposphere large scale circulation, namely the tropical westerlies are too

weak compared to ERA5 (not shown). The two biases (humidity and vorticity) are plausibly linked, but more work is needed to validate that hypothesis. By contrast, the potential intensity and velocity shear biases are small in the region of negative genesis density biases.

To summarize, both the vorticity and humidity biases resemble the WNP genesis density bias between ICO-VHR and ERA5 (see the thick dashed line on the third column panels of Fig. 12). It is well known that low vorticity and dry environments are both limiting factors for TC genesis, which suggests that these two biases may explain the reduced and northward shift of the TC's main development region in the WNP.

3.2.4 North Atlantic

By contrast with the WNP, our model shows a good ability to simulate the TC climatology of the NATL, as already discussed in Sect. 3.1.2. This is particularly true for the simulation ICO-VHR, for which TCs frequency, duration and seasonal cycle are close to the observations. Here, we further highlight their geographical distribution by showing zooms of the track density maps in the NATL for all resolutions and in the observations (Fig. 13). The general features of the observed geographical distributions are well captured for spatial resolutions equal to and finer than 100 km. For all simulations but ICO-LR, there is an excess of TCs in the Caribbean sea compared to the observations. In that part of the NATL, the number of TCs is almost constant for resolutions finer than 100 km. By contrast, there is a deficit of track density west of Africa in ICO-MR and ICO-HR. That deficit almost disappears in ICO-VHR. In fact, the number of TC tracks more than doubles between ICO-HR and ICO-VHR. It would be interesting to investigate further the origin of these different evolutions with spatial resolution in the different parts of the NATL. Such an investigation is beyond the scope of this paper. Rather, we stress that these small differences between the model results and the observations should not hide the main result of that section: TC activity in the NATL is spectacularly well captured in our simulations. This is particularly true for a spatial resolution of 25 km, but also holds to some extent for the coarser resolutions of 50 and 100 km. Such a good agreement is worth highlighting given that the North Atlantic basin TC activity is particularly difficult to simulate and is usually where most models have important biases (see e.g. Roberts et al. 2020).

In addition to TCs climatology, we have shown above that the model reproduces the observed interannual correlation between TC activity in the NATL and ENSO (see Sect. 3.2.1). This observed teleconnection has been shown in the literature to be mediated by the modulation of the large-scale environment by ENSO (Camargo et al. 2010). This section investigates whether this is also the case in our highest-resolution simulation.

To do so, we compare the interannual correlations found in the reanalysis between the ONI and the variables influencing TC genesis (Fig. 14, top row). All variables but the potential intensity display a significant correlation with the

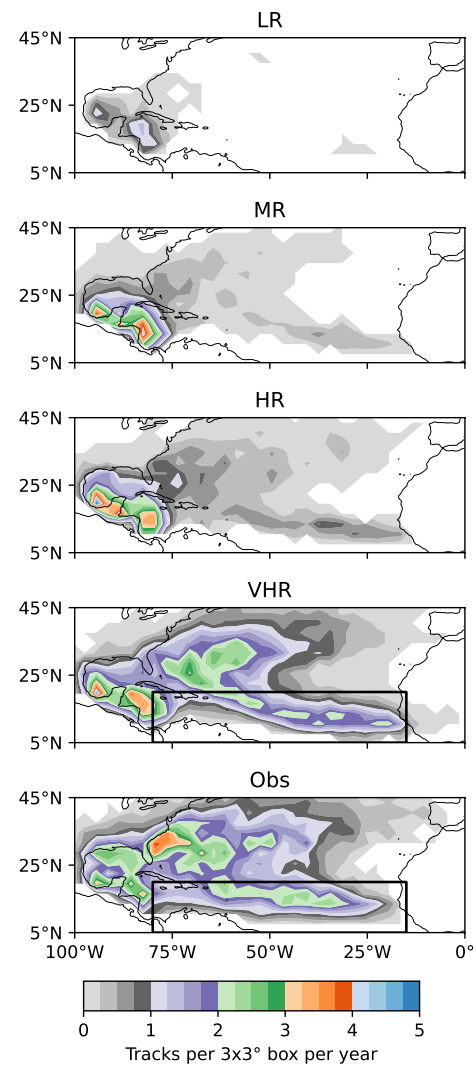
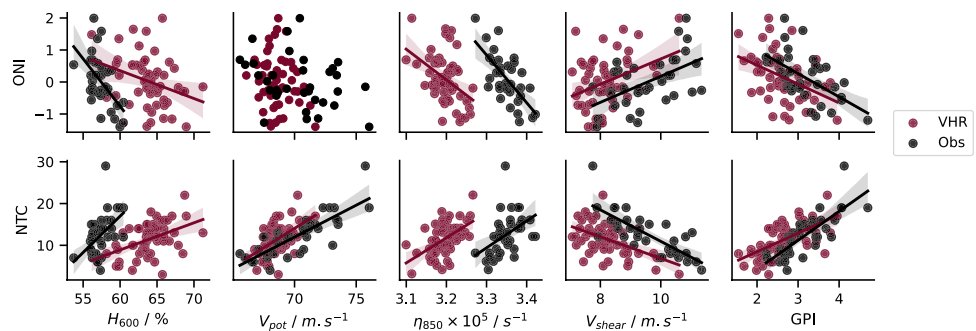


Fig. 13 Track density in the North Atlantic at each resolution and in IBTrACS. The box over which environmental variables were averaged for Fig. 14 ($5\text{--}20^{\circ}\text{N}/80\text{--}15^{\circ}\text{W}$) is overlaid on the panels VHR and Obs

ONI. This is true both in ERA5 and the model, although the correlation slope is smaller than observed in the model for relative humidity. Note that the latter displays a positive bias of about 10% compared to ERA5. There is also a negative relative vorticity bias apparent in the model, but the slope of the correlation in the model is the same as that found in ERA5. These relationships translate into a significant correlation between the GPI and the ONI: La-Niña years ($\text{ONI} < -0.5$) correspond to a more TC-favorable environment (large relative humidity and vorticity, weak shear, i.e., large GPI) than El-Niño. We conclude from this analysis that the model reproduces the teleconnection between ENSO and the large-scale environment in the NATL.

Additionally, all large-scale variables significantly correlate to TC frequency in the observations and the simulation

Fig. 14 Mean environmental fields in the MDR (5–20°N/80–15°W) against NTC and ONI index. Environmental fields and ONI are averaged yearly during the TC season (July to October included). Regression lines and associated confidence interval to 95% are displayed when the p -value associated with the two variables being correlated was below 5%



(Fig. 14, bottom row). The relationships between potential intensity and wind shear with NTC are closely reproduced. NTC is slightly less sensitive to humidity in the simulation than in the observations. This may be due to the humidity being too large in this region. Interestingly, NTC shows the same sensitivity to relative vorticity in the simulation as in the observations (the linear regressions have the same slope), despite the aforementioned negative bias of relative vorticity in the model. As a consequence, the GPI shows a similar correlation to NTC in the observations and the simulation. We found very similar results when making the same analysis using the ACE rather than TC frequency (not shown).

This analysis shows that the IPSL model at VHR resolution can reproduce the relationship that exists in the observations between the large-scale environment and TC activity. Moreover, it reproduces well the teleconnection between ENSO and the relevant large-scale fields in the NATL, hence the realistic correlation between ENSO and TC activity that was noted above in Sect. 3.2.1.

4 Conclusion and open issues

In this paper, we assessed the properties of tropical cyclones in the IPSL model by analyzing four HighResMIP atmosphere-only historical simulations with increasing spatial resolution. Such a systematic analysis constitutes the first global assessment of TC representation in the IPSL model. Although IPSL model simulations were included in several CMIP papers (Walsh et al. 2013; Camargo 2013; Tory et al. 2013), their ability to simulate TCs was not commented on specifically or was restricted to the NATL (Sainsbury et al. 2022). In addition, and by contrast with the present study, these papers were restricted to low resolution and coupled simulations. The main results we obtained are listed below:

- The IPSL model behaves as expected regarding the impact of increasing resolution. TC climatology and properties on global, regional, and local scales improve

as resolution is increased and compare favorably with observations for the finest resolution we considered.

- TC activity biases in the North Atlantic are very small at 25 km. In addition, the model is able to capture the links between the tropical large-scale environment and that activity, both climatologically and on interannual timescales.
- There is a significant deficit in cyclogenesis in the Western-North Pacific. It is likely associated with large-scale climatological biases of humidity and vorticity in the model.

The overall improvement of TC statistics and properties as resolution increases is in agreement with the main results of the few published papers that specifically tackled that question (Manganello et al. 2012; Strachan et al. 2013; Roberts et al. 2015, 2020). It clearly demonstrates that the IPSL model is a valuable tool to study TCs. This was the main goal of this work and this is its main conclusion.

An additional goal of our work was to highlight the strengths and weaknesses of the IPSL model as a tool to study TCs. The suite of simulations we presented above, with four consecutive two-fold increase in spatial resolution, reveals some of its specificities that are as many opportunities to help improve our understanding of TCs properties in simulations.

First, the lack of convergence of TC frequency with spatial resolution deserves further analysis. It immediately raises the question of whether the broad agreement we find with the observations at 25 km is fortuitous. Such a worry should be mitigated though. TC frequency is a very sensitive metric. Because it is discrete and characterized by rather low values, any missing cyclone or false alarm can have a significant impact on its value. Based on this argument, we should expect a strong sensitivity of TC frequency to the tracker used. Essentially, because each tracker sets a limit on the spectrum of tropical cyclones, and because TC intensity increases with resolution, a more selective tracker (e.g. UZ) is likely to converge for finer resolutions than a less selective one (e.g. TRACK). Roberts et al. (2020) indeed report larger increases of TC frequencies when using UZ

rather than TRACK in their HighResMIP multi-model comparison. Likewise, Strachan et al. (2013) used TRACK and found that TC frequencies converge in their model for spatial resolutions finer than 100 km. However, TC frequency convergence is not always found when using TRACK. Indeed, with that tracker, Roberts et al. (2015) and Manganello et al. (2012) both report increasing TC frequencies up to 25 and 10 km, respectively. Clearly, the reasons explaining these conflicting results should be better understood. Compared to the published results mentioned above, the IPSL model features an exacerbated sensitivity of the TC frequency to resolution, and particularly so between 50 and 25 km. Investigating this peculiar behavior may help progress on the issue of convergence of TC frequency with resolution.

Second, the small biases we found in the North Atlantic in the ICO-VHR simulations are noteworthy given the known and widely reported difficulties to correctly simulate TCs in that basin (Camargo 2013; Walsh et al. 2015; Roberts et al. 2020). Although increased spatial resolutions improves their representation, significant biases are often reported by the authors, even at the highest resolution (Manganello et al. 2012; Strachan et al. 2013; Roberts et al. 2015). The reasons explaining that improvement with resolution are not well understood. The large scale climatological biases in the NATL do not change dramatically with resolution and are thus unable to explain that behavior. This was also noted before by Roberts et al. (2015), who suggested that it could be due to the relationship between NATL TCs and African Easterly Waves being better represented at high resolution. However, that relationship itself is still being debated and the subject of intense research (Patricola et al. 2018; Bercos-Hickey et al. 2023). TC seeds are also important for TC properties (Vecchi et al. 2019; Sobel et al. 2021) and may be better captured at high resolution. The significant improvement with resolution of TC frequency and spatial distribution in the NATL found in the IPSL model provides an opportunity for future research on these possibilities.

Finally, we found a large bias of TC frequency in the WNP. Our analysis strongly suggests that it is related to a large-scale environment bias in the IPSL model that must be better understood and hopefully reduced. This last opportunity for future research might seem to be more oriented toward the IPSL community. This is true to some extent. However, such a bias of TC activity in the WNP is not uncommon and has been reported before (see e.g. Roberts et al. 2020). In fact, using nudging experiments, Wu et al. (2022) recently highlighted that a similar TC deficit in CAM could be alleviated by correcting a humidity bias that resembles ours.

It would be interesting to explore whether this is also the case in the IPSL model using similarly nudged numerical experiments. Progress on that issue will thus be beneficial for the entire community.

More generally, the very different behavior of the NATL and the WNP basins in the IPSL model is an opportunity to better understand the sensitivities of TCs properties to the model characteristics and in particular their respective relationships to the model parametrizations. It is indeed well known that TC activity is sensitive to several model parametrizations, including convection (Reed and Jablonowski 2011; Zhao et al. 2012; Kim et al. 2012; Lim et al. 2015), clouds (Vitart et al. 2001), and boundary layer momentum flux (Nardi et al. 2022b). This is likely the case in the IPSL model as well, and a detailed analysis of those sensitivities will be useful in this context.

Overall, our results and the above discussion demonstrate that the IPSL model is a suitable tool to study the properties and evolution of tropical cyclones on climate scales and to make progress on the open issues in that field.

Appendix 1: Impact of the dynamical core

In addition to the simulations presented in the main body of the paper, we also performed two simulations with the longitude-latitude native core of the LMDZ. These additional simulations also follow the HighResMIP protocol, and only differ in their spatial resolution. In this appendix we briefly document the similarities and differences we obtained in these simulations with the suite of simulations performed with DYNAMICO.

The original longitude-latitude core of the LMDZ (referred to as “Lon-Lat” hereafter) is a finite-difference/finite-volume solver for the primitive equations that uses a longitude-latitude “regular” grid. The resolution of the grid is defined by the number of cells in the latitudinal and longitudinal directions, noted $N_{lat} \times N_{lon}$. The two simulations discussed in this appendix use a resolution of 143×144 (LonLat-LR, $\mathcal{R} = 220$ km) and 361×512 (LonLat-HR, $\mathcal{R} = 73$ km). The small scale dissipation operators are identical in the Lon-Lat and ICO simulations. The associated timescales are equal in LonLat-LR and ICO-LR. On the other hand, to ensure stability, $\tau_{rot} = \tau_{\theta} = 900$ sec and $\tau_{div} = 600$ sec in LonLat-HR, i.e. smaller than the corresponding values in ICO-HR (Table 5).

NTC, TCD, and ACE are reported in Table 2 for the two Lon-Lat simulations and are plotted against \mathcal{R} in Fig. 15 for

Table 5 Same as Table 2, but for the simulations performed with the LMDZ native core

Simulation	Grid	\mathcal{R} (km)	NTC	TCD	ACE
LonLat-LR	143×144	220	2.2	13	0.7
LonLat-HR	361×512	73	35.1	236	21
Obs			88	776	179

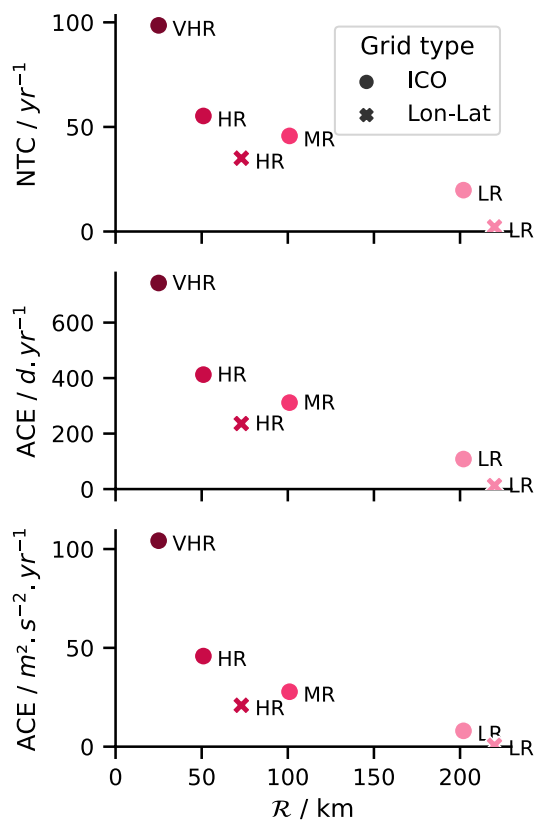


Fig. 15 TC activity metrics for each simulation. Color corresponds to nominal resolution, marker to the type of grid used

the six simulations we consider in this paper. As discussed above for the simulations using DYNAMICO, we recover the result for the Lon–Lat core that TC activity decreases as the spatial resolution gets coarser. In addition, for a given nominal resolution (LR or HR), all three metrics are lower with the Lon–Lat core than with DYNAMICO. Maximum wind speeds are larger for the ICO–HR simulation (Mean 20 m s^{-1}) than for the LonLat–HR simulation (Mean 18 m s^{-1}). These quantitative differences in TCs frequencies and strength between the two dynamical cores can be explained by two reasons:

1. The effective resolution in the tropics is coarser with the longitude–latitude grid than with the icosahedral grid for the same nominal resolution. For example, $R = 73 \text{ km}$ in the LonLat–HR simulation and only 51 km in the ICO–HR simulation.
2. The artificial dissipation used in the LonLat–HR simulation is larger than ICO–HR (this was set to ensure stability). This difference may lead to a larger damping of strong winds and hinder the formation and intensification of TCs in LonLat–HR. This may also explain why the three metrics in the LonLat–HR simulation are

lower than those found in the ICO–MR simulation, even though the spatial resolution of the latter is coarser.

To summarize, we find comparable global climatologies when using the two dynamical cores of the IPSL model. This result might appear to disagree with Reed et al. (2015), who found a significant change in frequency and intensity when comparing the results obtained with two dynamical cores. It must be noted however that the two dynamical cores we tested in the present study are more similar than theirs: DYNAMICO and the longitude–latitude grid of the IPSL model are both finite differences cores, they mainly differ in their grid, whereas Reed et al. (2015) compared a finite-volume core and a spectral element core.

It is also encouraging to see that the use of DYNAMICO positively impacts both TC activity and maximum intensity. However, the observed positive impact of decreasing the small scale dissipation that is suggested by the data seems to contradict results published in the literature. Indeed, both Zhao et al. (2012) and Reed et al. (2015) report that TCs frequencies and strengths increase with dissipation. More work is required to confirm and better understand the sensitivity of modelled TCs to small scale dissipation in climate models.

Appendix 2: Regional analysis

In this appendix, we detail the impact of increasing resolution in each of the eight TC basins, in terms of frequency, duration, intensity, seasonal cycle, and geographical distribution. This description is made in comparison with observations in IBTrACS, and based on the Figs. 5, 16, 17, 18, 19, and 6. They show the TC activity metrics, and distributions of duration, minimum lifetime SLP, maximum lifetime surface wind speed, seasonal cycles, and geographical distribution for each basin respectively. Basins are described in order of decreasing frequency, with the exception of the CP, which is inserted after the two north Pacific basins.

Western North Pacific (WNP)

Frequency

Activity is very low in ICO–LR, ICO–MR, and ICO–HR, with less than 7 TCs per year (Fig. 5). There is a marked increase in ICO–VHR up to 19 TCs per year, although not large enough to catch up with the observed level (26 TCs per year).

Duration

The WNP features the longest track duration of all basins, with an average of 8.7 days in ICO–VHR. However, the

Fig. 16 Duration distribution in each basin for each resolution

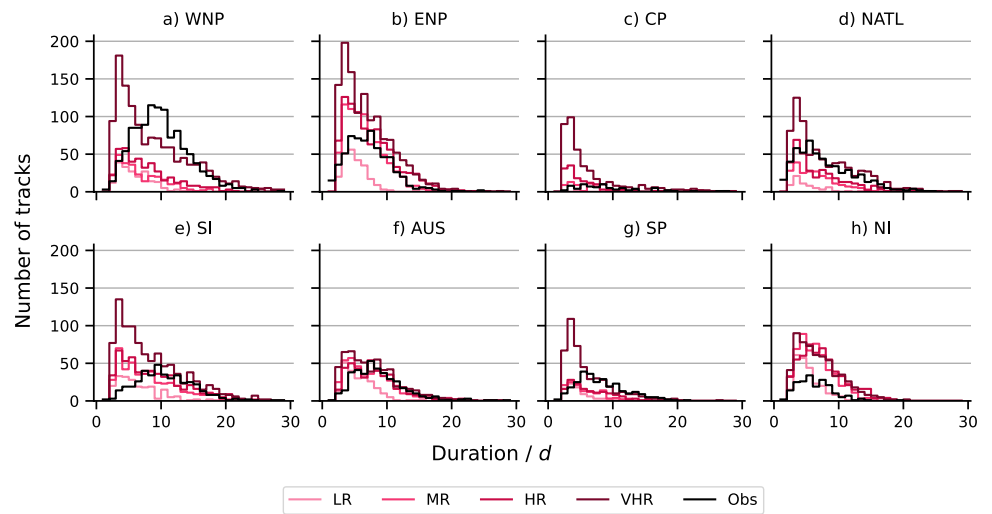


Fig. 17 Minimum lifetime SLP distribution in each basin for each resolution

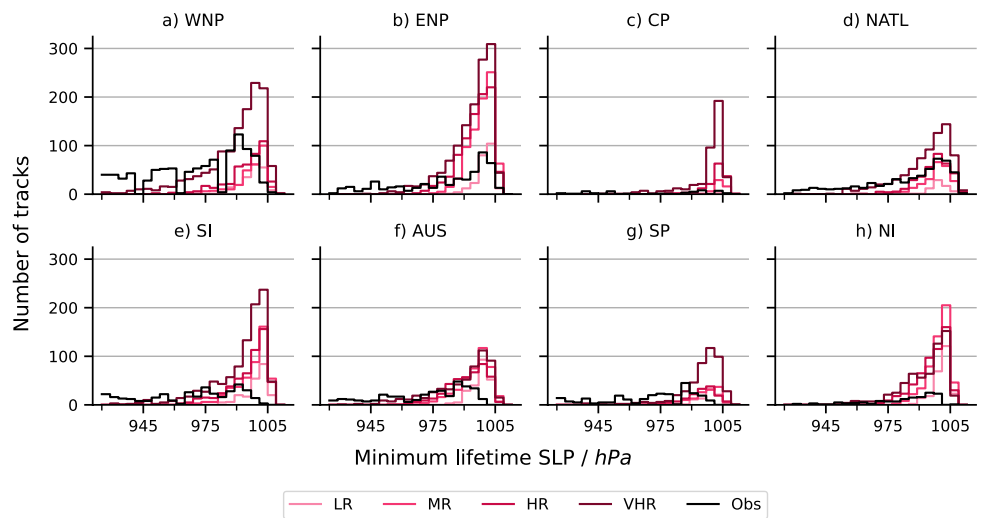


Fig. 18 Maximum lifetime surface wind speed distribution in each basin for each resolution

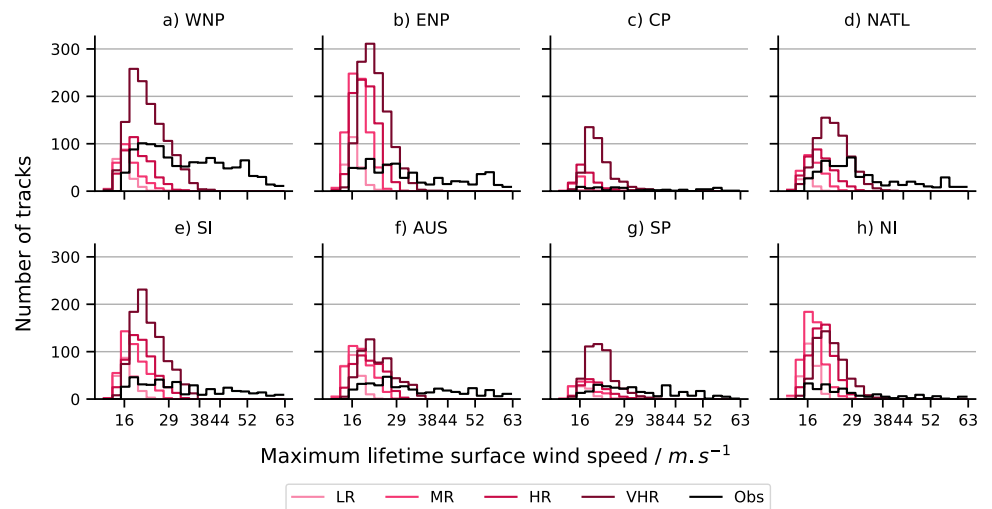
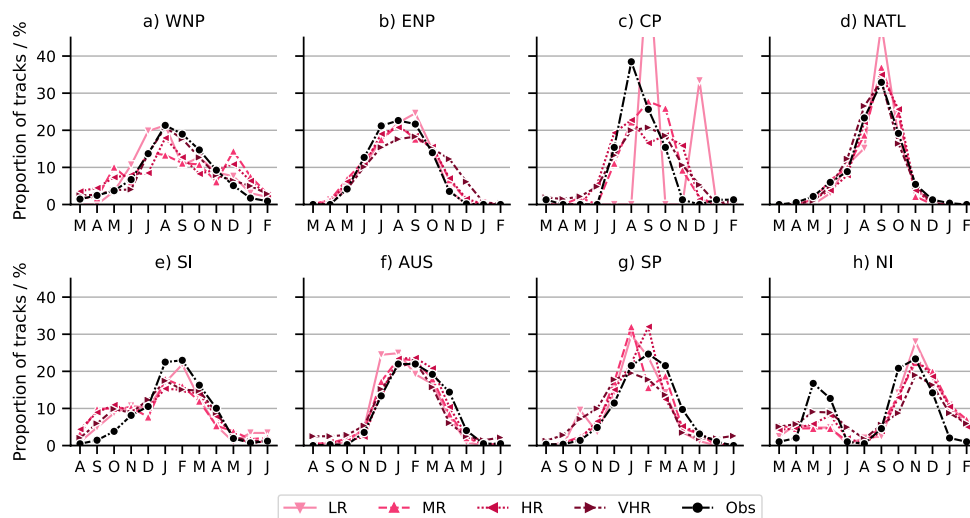


Fig. 19 Seasonal cycle in each basin for each resolution compared to the observations. TCs are binned according to the month during which they reach their lifetime maximum intensity, as measured in terms of minimum SLP and excluding ET points



duration distribution shows a large number of short tracks. (Fig. 16a).

Intensity

TCs in the WNP are intense: In ICO-HR and ICO-VHR, respectively, 33 and 39% of category 3 and more TCs are found in the WNP, compared to 39% in the observations (not shown).

Seasonal cycle

The peak activity occurs in August in the simulations, in agreement with the observations (Fig. 19a). We note the existence of some off-season tracks, which are mainly of short duration (not shown).

Geographical distribution

In ICO-VHR, TC genesis is biased northward compared to the observations. The maximum genesis occurs along the 20°N parallel instead of 10°N (Fig. 6). Activity is also too uniformly distributed in longitude.

Eastern North Pacific (ENP)

Frequency

The ENP features a steep increase in frequency between ICO-LR (4 yr⁻¹) and ICO-MR (13 yr⁻¹), but a comparatively smaller increase for the higher resolutions simulations ICO-HR (14 yr⁻¹) and ICO-VHR (19 yr⁻¹) (Fig. 5).

Duration

The average duration is close to that observed (7 days), but it must be noted that there are too few (resp. too much) long (resp. short) tracks (Fig. 16b).

Intensity

Simulated TCs rarely exceed SSHS wind category 2, in agreement with the observations (Fig. 18b).

Seasonal cycle

The seasonal cycle is well captured at every resolution, despite some additional tracks in November and December in ICO-VHR (Fig. 19b).

Geographical distribution

The observed activity in the ENP is concentrated close to the Central America coastline (Fig. 6). This is also the case in the simulations. However, there is a secondary maximum in ICO-MR, ICO-HR, and ICO-VHR close to the coast of Guatemala (around 13°N–93°W) not present in the observations.

Central Pacific (CP)

Frequency

The number of TCs in the simulations is very sensitive to spatial resolution: There is none in ICO-LR, a few in

ICO-MR and ICO-HR, and three times as many in ICO-VHR as in the observations (2 TCs per year, Fig. 5).

Duration

Because it is a wide open sea, the few observed TCs in the CP last for a long time (9.2 days on average), whereas simulated TCs last on average 6.5 days, which is the second lowest duration globally.

Intensity

TCs in the CP are mainly weak, scarcely reaching category 1 neither in SLP nor in wind speed (Figs. 18c and 17c).

Seasonal cycle

The TC season lasts from July to November, i.e., longer than in the observations. However, as in the observations, there is strictly no simulated TC from January to May. (Fig. 19c)

Geographical distribution

In ICO-VHR, the main feature is a continuous band of genesis and track density from the dateline to 105°W that is unseen in the observations (Fig. 6).

North ATLantic (NATL)

Frequency

TC activity regularly builds up with increasing resolution. In ICO-VHR, the simulated TC frequency (12 yr⁻¹) is close to that observed (14 yr⁻¹) (Fig. 5).

Duration

The average duration of TC tracks in ICO-VHR is the same as the observations: 7.7 days. It is only slightly lower at lower resolutions. However, as in most other basins, there is a peak of short tracks in ICO-HR and ICO-VHR (Fig. 16d).

Intensity

Intensity increases with resolution. In ICO-VHR, the number of TC in categories 0–1 is overestimated. In category 2, it is well simulated, and in categories 3 and more, it is underestimated (Figs. 18d and 17d).

Seasonal cycle

The peak is too strong at low resolution compared to the observations. However, the simulated seasonal cycle is

almost indistinguishable from the observed one for finer resolutions. (Fig. 19d)

Geographical distribution

Genesis in the North Atlantic occurs mainly off the coast of Africa around 12°N, in an area called, for this reason, the Main Development Region (MDR), with a secondary maximum in the Caribbean Sea. This pattern is well reproduced in the ICO-VHR simulation. At lower resolutions, the Caribbean Sea relative contribution is stronger than that of the MDR. In the observations, TC activity is distributed along a curve from the coast of Africa to the Antilles, along the East coast of the USA, and in the Caribbean Sea. These features are particularly well reproduced in ICO-VHR (Figs. 6 and 13).

South Indian (SI)

Frequency

TC activity increase with spatial resolution is reminiscent of that observed at the global scale, with a twofold increase between ICO-LR and ICO-MR, and between ICO-HR and ICO-VHR, with comparatively small differences between the ICO-MR and ICO-HR. We find a positive bias in ICO-VHR (15 yr⁻¹) compared to the observations (10 yr⁻¹) (Fig. 5)

Duration

As in several other basins, TC durations display an excess of short tracks (Fig. 16e).

Intensity

A few TCs reach up to category 4 intensity in terms of SLP (Fig. 17e).

Seasonal cycle

The cyclonic season starts too early in the simulations (August/September) compared to the observations (October/November), regardless of the resolution (Fig. 19e).

Geographical distribution

While activity is concentrated in the east of the basin at lower resolutions, TCs reach Madagascar and the Gulf of Mozambique in ICO-VHR, in better agreement with the observations (Fig. 6).

Australian basin (AUS)

Frequency

TC frequency is already significant in ICO-MR (7 yr^{-1}) and only displays a modest increase at higher resolution. The simulated TC frequency in ICO-VHR (9 yr^{-1}) almost matches the observed frequency (10 yr^{-1}) (Fig. 5)

Duration and intensity

There is an excess of short and weak tracks in ICO-HR and ICO-VHR compared to lower spatial resolutions (Figs. 16f, 18f, and 17f).

Seasonal cycle

For all resolutions, the seasonal cycle agrees with the observations (Fig. 19f).

Geographical distribution

In ICO-LR, ICO-MR, and ICO-HR, activity is concentrated along the Western Australian coast. At the same time, it shows a better East-West balance in ICO-VHR compared to the observations (Fig. 6).

South Pacific (SP)

Frequency

TC frequency is low in ICO-LR, ICO-MR and ICO-HR ($\sim 2 \text{ yr}^{-1}$) and only reaches observed levels in ICO-VHR (7 yr^{-1}) (Fig. 5)

Duration and intensity

Almost all tracks in ICO-VHR are too short and too weak compared to the observations (Figs. 16g, 18g, and 17g).

Seasonal cycle

The ICO-VHR seasonal cycle is shifted earlier by about one month compared to the observations (Fig. 19g). As a result, the peak occurs in January and not in February. Furthermore, it is underestimated compared to the observations, while we find an excess of TCs in the early part of the cyclonic season (September to December). It is

noisier at lower resolutions due to the limited sample sizes available for those cases.

Geographical distribution

In agreement with the observations, the simulated activity in ICO-VHR is concentrated on the western side of the basin, with no TC of the coast of South America (Fig. 6).

North Indian (NI)

Most models in HighResMIP overestimate TC frequency in the NI (Roberts et al. 2020), and that basin is sometimes even removed from the analyses because of the interaction between TCs and the monsoon, making detection difficult. In our simulation, the NI also stands out as an outlier.

Frequency

The simulated TC frequency is at the observed level in ICO-LR ($\sim 5 \text{ yr}^{-1}$), and twice as large in ICO-MR, ICO-HR, and ICO-VHR, with the later three simulations showing very little differences (Fig. 5).

Duration

Tracks are longer than observed because they are detected further inland (Fig. 16h). It is difficult to know whether it is a feature of the tracking methodology or whether the models fails at simulating quick dissipation over land.

Intensity

Similarly to the observations, NI simulated TCs rarely exceed category 2 (Figs. 18h and 17h).

Seasonal cycle

The seasonal cycle in the simulations displays a clear minimum in summer during the monsoon and a maximum in October-November. However, the season extends into the winter, only shows a marginal decrease in activity in March, and starts again in April. This is not in accordance with the observations, that display a clear secondary peak of activity in May and June (Fig. 19h).

Geographical distribution

In the observations, one-third of the TCs appear in the Arabian Sea (AS), and two-thirds in the Gulf of Bengal (GB). Such a distribution is best reproduced in ICO-MR (Fig. 6). By contrast, most TCs appear in the GB in ICO-LR, while TC proportion increases in favor of the AS in ICO-HR

and ICO-VHR, to the point that there are nearly as many TCs in the GB and the AS in the ICO-VHR simulation (not shown).

Supplementary Information The online version contains supplementary material available at <https://doi.org/10.1007/s00382-024-07138-w>.

Acknowledgements The authors would like to thank Suzana Camargo and two anonymous reviewers for their thorough review of the manuscript. The research is supported by public funding. S. Bourdin and S. Fromang were financially supported by the CEA, by the EUR IPSL-Climate Graduate School through the ICOCYCLONES and ICOCYCLONES2 projects, managed by the ANR under the “Investissements d’avenir” programme with the reference ANR-11-IDEX-0004-17-EURE-0006, and by the IS-ENES project. The TGCC and the IPSL Data and Computing Center ESPRI provided simulation and data processing infrastructure. Figures were designed using Python, in particular the matplotlib, cartopy and seaborn packages.

Author contributions SB and SF designed the study. YM and TD developed the new dynamical core. AC and JG ran the simulations. SB conducted the analyses under SF’s supervision and with YM’s advice. SB and SF wrote the manuscript.

Funding The authors have not disclosed any funding.

Data availability The HighResMIP simulations are available through ESGF at <https://esgf-node.ipsl.upmc.fr/projects/cmip6-ipsl/>. ERA5 data is available on the Climate Data Store <https://cds.climate.copernicus.eu/>. IBTrACS is available online at <https://www.ncei.noaa.gov/products/international-best-track-archive>. ONI time series was retrieved from <https://www.cpc.ncep.noaa.gov/data/indices/oni.ascii.txt>. Additional data was stored on Zenodo (<https://doi.org/10.5281/zenodo.8202411>): (1) TC tracks in all the simulations before and after the STJ filtering; (2) Composite NetCDFs; (3) Large scale variables used in the GPI, and the GPI itself, in ICO-VHR and ERA5.

Declarations

Conflict of interest The authors declare no conflict of interest.

Open Access This article is licensed under a Creative Commons Attribution 4.0 International License, which permits use, sharing, adaptation, distribution and reproduction in any medium or format, as long as you give appropriate credit to the original author(s) and the source, provide a link to the Creative Commons licence, and indicate if changes were made. The images or other third party material in this article are included in the article’s Creative Commons licence, unless indicated otherwise in a credit line to the material. If material is not included in the article’s Creative Commons licence and your intended use is not permitted by statutory regulation or exceeds the permitted use, you will need to obtain permission directly from the copyright holder. To view a copy of this licence, visit <http://creativecommons.org/licenses/by/4.0/>.

References

- Bardet D, Spiga A, Guerlet S, Cabanes S, Millour E, Boissinot A (2021) Global climate modeling of Saturn’s atmosphere. Part IV: Stratospheric equatorial oscillation, vol 354, p 114042. <https://doi.org/10.1016/j.icarus.2020.114042>. arXiv:2001.07009 [physics.aos-ph]
- Bardet D, Spiga A, Guerlet S (2022) Joint evolution of equatorial oscillation and interhemispheric circulation in Saturn’s stratosphere. *Nat Astron* 6:804–811. <https://doi.org/10.1038/s41550-022-01670-7>
- Befort DJ, Hodges KI, Weisheimer A (2022) Seasonal prediction of tropical cyclones over the North Atlantic and Western North Pacific. *J Clim* 35(5):1385–1397
- Bercos-Hickey E, Patricola CM, Loring B, Collins WD (2023) The relationship between African easterly waves and tropical cyclones in historical and future climates in the HighResMIP-PRIMAVERA simulations. *J Geophys Res (Atmos)* 128(7):2022–037471. <https://doi.org/10.1029/2022JD037471>
- Boucher O, Servonnat J, Albright AL, Aumont O, Balkanski Y, Bastrikov V, Bekki S, Bonnet R, Bony S, Bopp L, Braconnot P, Brockmann P, Cadule P, Caubel A, Cheruy F, Codron F, Cozic A, Cugnet D, D’Andrea F, Davini P, Lavergne C, Denvil S, Deshayes J, Devilliers M, Ducharne A, Dufresne J-L, Dupont E, Étché C, Fairhead L, Falletti L, Flavoni S, Foujols M-A, Gardoll S, Gastineau G, Ghattas J, Grandpeix J-Y, Guenet B, Lionel Guez E, Guilyardi E, Guimberteau M, Hauglustaine D, Hourdin F, Idelkadi A, Joussaume S, Kageyama M, Khodri M, Krinner G, Lebas N, Levvasseur G, Lévy C, Li L, Lott F, Lurton T, Luysaert S, Madec G, Madeleine J-B, Maignan F, Marchand M, Marti O, Mellul L, Meurdesoif Y, Mignot J, Musat I, Ottlé C, Peylin P, Planton Y, Polcher J, Rio C, Rochetin N, Rousset C, Sepulchre P, Sima A, Swingedouw D, Thiéblemont R, Traore AK, Vancoppenolle M, Vial J, Vialard J, Viovy N, Vuichard N (2020) Presentation and evaluation of the IPSL-CM6A-LR climate model. *J Adv Model Earth Syst*. <https://doi.org/10.1029/2019MS002010>
- Bourdin S, Fromang S, Dulac W, Cattiaux J, Chauvin F (2022) Inter-comparison of four algorithms for detecting tropical cyclones using ERA5. *Geosci Model Develop*. <https://doi.org/10.5194/gmd-15-6759-2022>
- Cabanes S, Spiga A, Young RMB (2020) Global climate modeling of Saturn’s atmosphere. Part III: global statistical picture of zonal-turbulence in high-resolution 3D-turbulent simulations, vol 345, p 113705. <https://doi.org/10.1016/j.icarus.2020.113705>
- Camargo SJ (2013) Global and regional aspects of tropical cyclone activity in the CMIP5 models. *J Clim*. <https://doi.org/10.1175/JCLI-D-12-00549.1>
- Camargo SJ, Wing AA (2016) Tropical cyclones in climate models. *WIREs Clim Change*. <https://doi.org/10.1002/wcc.373>
- Camargo SJ, Sobel AH, Barnston AG, Klotzbach PJ (2010) The influence of natural climate variability on tropical cyclones, and seasonal forecasts of tropical cyclone activity. In: *Global perspectives on tropical cyclones*. World Scientific Series on Asia-Pacific Weather and Climate, vol 4, pp 325–360. World Scientific, Singapore. https://doi.org/10.1142/9789814293488_0011. https://www.worldscientific.com/doi/abs/10.1142/9789814293488_0011. Accessed 2023-02-13
- Cattiaux J, Chauvin F, Bousquet O, Malardel S, Tsai C-L (2020) Projected changes in the Southern Indian ocean cyclone activity assessed from high-resolution experiments and CMIP5 models. *J Clim*. <https://doi.org/10.1175/JCLI-D-19-0591.1>
- Chavas DR, Reed KA, Knaff JA (2017) Physical understanding of the tropical cyclone wind-pressure relationship. *Nat Commun*. <https://doi.org/10.1038/s41467-017-01546-9>
- Dubos T, Dubey S, Tort M, Mittal R, Meurdesoif Y, Hourdin F (2015) DYNAMICO-1.0, an icosahedral hydrostatic dynamical core designed for consistency and versatility. *Geosci Model Develop*. <https://doi.org/10.5194/gmd-8-3131-20158>
- Dulac W, Cattiaux J, Chauvin F, Bourdin S, Fromang S (2023) Assessing the representation of tropical cyclones in era5 with the CNRM tracker. *Clim Dyn* 2023:1–16

- Emanuel KA (2003) Tropical cyclones. *Ann Rev Earth Planet Sci* 31(1):75–104
- Emanuel KA, Nolan DS (2004) Tropical cyclone activity and the global climate system. In: 26th Conference on hurricanes and tropical meteorology, pp 240–241
- Emanuel KA (2018) 100 years of progress in tropical cyclone research. *Meteorol Monogr*. <https://doi.org/10.1175/AMSMONOGRAPHS-D-18-0016.1>
- Gray WM (1975) Tropical cyclone genesis in the western north pacific. *J Meteorol Soc Jpn Ser II* 55:465–482
- Gray WM (1979) Hurricanes: their formation, structure and likely role in the tropical circulation. *Meteorology over the tropical oceans*. *R Meteorol Soc* 1979:155–218
- Haarsma RJ, Roberts MJ, Vidale PL, Senior CA, Bellucci A, Bao Q, Chang P, Corti S, Fučkar NS, Guemas V, Hardenberg J, Hazleger W, Kodama C, Koenigk T, Leung LR, Lu J, Luo J-J, Mao J, Mizielinski MS, Mizuta R, Nobre P, Satoh M, Scoccimarro E, Semmler T, Small J, Storch J-S (2016) High resolution model intercomparison project (HighResMIP v1.0) for CMIP6. *Geosci Model Develop* 9(11):1
- Horn M, Walsh K, Zhao M, Camargo SJ, Scoccimarro E, Murakami H, Wang H, Ballinger A, Kumar A, Shaevitz DA, Jonas JA, Oouchi K (2014) Tracking scheme dependence of simulated tropical cyclone response to idealized climate simulations. *J Clim*. <https://doi.org/10.1175/JCLI-D-14-00200.1>
- Hourdin F, Rio C, Grandpeix J-Y, Madeleine J-B, Cheruy F, Rochetin N, Jam A, Musat I, Idelkadi A, Fairhead L, Foujols M-A, Mellul L, Traore A-K, Dufresne J-L, Boucher O, Lefebvre M-P, Millour E, Vignon E, Jouhaud J, Diallo FB, Lott F, Gastineau G, Caubel A, Meurdesoif Y, Ghattas J (2020) LMDZ6A: the atmospheric component of the IPSL climate model with improved and better tuned physics. *J Adv Model Earth Syst*. <https://doi.org/10.1029/2019MS001892>
- Kim D, Sobel AH, Genio ADD, Chen Y, Camargo SJ, Yao M-S, Kelley M, Nazarenko L (2012) The tropical subseasonal variability simulated in the NASA GISS general circulation model. *J Clim*. <https://doi.org/10.1175/JCLI-D-11-00447.1>
- Klotzbach PJ, Bell MM, Bowen SG, Gibney EJ, Knapp KR, Schreck CJ (2020) Surface pressure a more skillful predictor of normalized hurricane damage than maximum sustained wind. *Bull Am Meteorol Soc*. <https://doi.org/10.1175/BAMS-D-19-0062.1>
- Knapp KR, Kruk MC, Levinson DH, Diamond HJ, Neumann CJ (2010) The international best track archive for climate stewardship (IBTrACS): unifying tropical cyclone data. *Bull Am Meteorol Soc*. <https://doi.org/10.1175/2009BAMS2755.1>
- Knapp KR, Diamond HJ, Kossin JP, Kruk MC Schreck C et al (2018) International best track archive for climate stewardship (ibtracs) project, version 4. <https://doi.org/10.25921/82ty-9e16>. Accessed 2023-01-08
- Knutson TR, Sirutis JJ, Zhao M, Tuleya RE, Bender M, Vecchi GA, Villarini G, Chavas D (2015) Global projections of intense tropical cyclone activity for the late twenty-first century from dynamical downscaling of CMIP5/RCP45 scenarios. *J Clim*. <https://doi.org/10.1175/JCLI-D-15-0129.1>
- Li J-LF, Xu K-M, Richardson M, Jiang JH, Stephens G, Lee W-L, Fetzer E, Yu J-Y, Wang Y-H, Wang F (2021) Improved ice content, radiation, precipitation and low-level circulation over the tropical pacific from eCMWF era-interim to era5. *Environ Res Commun* 3(8):081006
- Lim Y-K, Schubert SD, Reale O, Lee M-I, Molod AM, Suarez MJ (2015) Sensitivity of tropical cyclones to parameterized convection in the NASA GEOS-5 model. *J Clim*. <https://doi.org/10.1175/JCLI-D-14-00104.1>
- Mallen KJ, Montgomery MT, Wang B (2005) Reexamining the near-core radial structure of the tropical cyclone primary circulation: implications for vortex resiliency. *J Atmos Sci* 62(2):408–425
- Manganello JV, Hodges KI, Kinter JL, Cash BA, Marx L, Jung T, Achuthavarier D, Adams JM, Altshuler EL, Huang B, Jin EK, Stan C, Towers P, Wedi N (2012) Tropical cyclone climatology in a 10-km global atmospheric GCM: toward weather-resolving climate modeling. *J Clim*. <https://doi.org/10.1175/JCLI-D-11-00346.1>
- McBride JL, Zehr R (1981) Observational analysis of tropical cyclone formation. Part II: comparison of non-developing versus developing systems. *J Atmos Sci* 1981:1132–1151
- Moon Y, Kim D, Camargo SJ, Wing AA, Sobel AH, Murakami H, Reed KA, Scoccimarro E, Vecchi GA, Wehner MF, Zarzycki CM, Zhao M (2020) Azimuthally averaged wind and thermodynamic structures of tropical cyclones in global climate models and their sensitivity to horizontal resolution. *J Clim*. <https://doi.org/10.1175/JCLI-D-19-0172.1>
- Nardi KM, Zarzycki CM, Larson VE, Bryan GH (2022a) Assessing the sensitivity of the tropical cyclone boundary layer to the parameterization of momentum flux in the community earth system model. *Monthly Weather Rev*. <https://doi.org/10.1175/MWR-D-21-0186>
- Nardi KM, Zarzycki CM, Larson VE, Bryan GH (2022b) Assessing the sensitivity of the tropical cyclone boundary layer to the parameterization of momentum flux in the community earth system model. *Monthly Weather Rev* 150(4):883–906
- Patricola CM, Saravanan R, Chang P (2018) The response of Atlantic tropical cyclones to suppression of African easterly waves. *Geophys Res Lett*. <https://doi.org/10.1002/2017GL076081>
- Reed KA, Jablonowski C (2011) Impact of physical parameterizations on idealized tropical cyclones in the community atmosphere model. *Geophys Res Lett*. <https://doi.org/10.1029/2010GL046297>
- Reed KA, Bacmeister JT, Rosenbloom NA, Wehner MF, Bates SC, Lauritzen PH, Truesdale JE, Hannay C (2015) Impact of the dynamical core on the direct simulation of tropical cyclones in a high-resolution global model. *Geophys Res Lett*. <https://doi.org/10.1002/2015GL063974>
- Roberts MJ, Vidale PL, Mizielinski MS, Demory M-E, Schiemann R, Strachan J, Hodges K, Bell R, Camp J (2015) Tropical cyclones in the UPSCALE ensemble of high-resolution global climate models. *J Clim*. <https://doi.org/10.1175/JCLI-D-14-00131.1>
- Roberts MJ, Camp J, Seddon J, Vidale PL, Hodges K, Vanniere B, Mecking J, Haarsma R, Bellucci A, Scoccimarro E, Caron L-P, Chauvin F, Terray L, Valcke S, Moine M-P, Putrasahan D, Roberts C, Senan R, Zarzycki C, Ullrich P (2020) Impact of model resolution on tropical cyclone simulation using the HighResMIP-PRIMAVERA multimodel ensemble. *J Clim*. <https://doi.org/10.1175/JCLI-D-19-0639.1>
- Roberts MJ, Camp J, Seddon J, Vidale PL, Hodges K, Vannière B, Mecking J, Haarsma R, Bellucci A, Scoccimarro E, Caron L-P, Chauvin F, Terray L, Valcke S, Moine M-P, Putrasahan D, Roberts CD, Senan R, Zarzycki C, Ullrich P, Yamada Y, Mizuta R, Kodama C, Fu D, Zhang Q, Danabasoglu G, Rosenbloom N, Wang H, Wu L (2020) Projected future changes in tropical cyclones using the CMIP6 HighResMIP multimodel ensemble. *Geophys Res Lett*. <https://doi.org/10.1029/2020GL088662>
- Roberts MJ, Jackson LC, Roberts CD, Meccia V, Docquier D, Koenigk T, Ortega P, Moreno-Chamarro E, Bellucci A, Coward A, Drijfhout S, Exarchou E, Gutjahr O, Hewitt H, Iovino D, Lohmann K, Putrasahan D, Schiemann R, Seddon J, Terray L, Xu X, Zhang Q, Chang P, Yeager SG, Castruccio FS, Zhang S, Wu L (2020) Sensitivity of the atlantic meridional overturning circulation to model resolution in CMIP6 HighResMIP simulations and implications for future changes. *J Adv Model Earth Syst*. <https://doi.org/10.1029/2019MS002014>
- Ropelewski CF, Jones PD (1987) An extension of the Tahiti-Darwin southern oscillation index. *Monthly Weather Rev* 115(9):2161–2165

- Royer J-F, Chauvin F, Timbal B, Araspin P, Grimal D (1998) A GCM study of the impact of greenhouse gas increase on the frequency of occurrence of tropical cyclones. *Clim Change* 38(3):307–343
- Sainsbury EM, Schiemann RKH, Hodges KI, Baker AJ, Shaffrey LC, Bhatia KT, Bourdin S (2022) Can low-resolution CMIP6 ScenarioMIP models provide insight into future European post-tropical-cyclone risk? *Weather Clim Dyn*. <https://doi.org/10.5194/wcd-3-1359-2022>
- Smith RK, Montgomery MT (2023) Tropical cyclones, volume 4—1st Edition, Royal meteorological society edn. *Developments in Weather and Climate Science*, vol 4. Elsevier, London. <https://shop.elsevier.com/books/tropical-cyclones/smith/978-0-443-13449-4>. Accessed 2023-11-14
- Sobel AH, Wing AA, Camargo SJ, Patricola CM, Vecchi GA, Lee C-Y, Tippett MK (2021) Tropical cyclone frequency. *Earth Fut*. <https://doi.org/10.1029/2021EF002275>
- Spiga A, Guerlet S, Millour E, Indurain M, Meurdesoif Y, Cabanes S, Dubos T, Leconte J, Boissinot A, Lebonnois S, Sylvestre M, Fouchet T (2020) Global climate modeling of Saturn's atmosphere. Part II: multi-annual high-resolution dynamical simulations, vol 335, p 113377. <https://doi.org/10.1016/j.icarus.2019.07.011>. [arXiv:1811.01250](https://arxiv.org/abs/1811.01250) [astro-ph.EP]
- Strachan J, Vidale PL, Hodges K, Roberts M, Demory M-E (2013) Investigating global tropical cyclone activity with a hierarchy of AGCMs: the role of model resolution. *J Clim*. <https://doi.org/10.1175/JCLI-D-12-00012.1>
- Tippett MK, Camargo SJ, Sobel AH (2011) A Poisson regression index for tropical cyclone genesis and the role of large-scale vorticity in genesis. *J Clim* 24(9):2335–2357
- Tory KJ, Chand SS, McBride JL, Ye H, Dare RA (2013) Projected changes in late-twenty-first-century tropical cyclone frequency in 13 coupled climate models from phase 5 of the coupled model intercomparison project. *J Clim*. <https://doi.org/10.1175/JCLI-D-13-00010.1>
- Trenberth KE (2020) Enso in the global climate system. *El Niño Southern Oscillation in a Changing Climate*, pp 21–37
- Ullrich PA, Zarzycki CM (2017) TempestExtremes: a framework for scale-insensitive pointwise feature tracking on unstructured grids. *Geosci Model Develop*. <https://doi.org/10.5194/gmd-10-1069-2017>
- Ullrich PA, Zarzycki CM, McClenny EE, Pinheiro MC, Stansfield AM, Reed KA (2021) TempestExtremes v2.1: a community framework for feature detection, tracking and analysis in large datasets. *Geosci Model Develop Discuss*. <https://doi.org/10.5194/gmd-2020-303>
- Vannière B, Roberts M, Vidale PL, Hodges K, Demory M-E, Caron L-P, Scoccimarro E, Terray L, Senan R (2020) The moisture budget of tropical cyclones in HighResMIP models: large-scale environmental balance and sensitivity to horizontal resolution. *J Clim*. <https://doi.org/10.1175/JCLI-D-19-0999.1>
- Vecchi GA, Delworth TL, Murakami H, Underwood SD, Wittenberg AT, Zeng F, Zhang W, Baldwin JW, Bhatia KT, Cooke W, He J, Kapnick SB, Knutson TR, Villarini G, Wiel K, Anderson W, Balaji V, Chen J, Dixon KW, Gudgel R, Harris LM, Jia L, Johnson NC, Lin S-J, Liu M, Ng CHJ, Rosati A, Smith JA, Yang X (2019) Tropical cyclone sensitivities to CO₂ doubling: roles of atmospheric resolution, synoptic variability and background climate changes. *Clim Dyn* 53(9):5999–6033. <https://doi.org/10.1007/s00382-019-04913-y>
- Vitart F, Anderson JL, Sirutis J, Tuleya RE (2001) Sensitivity of tropical storms simulated by a general circulation model to changes in cumulus parametrization. *Quart J R Meteorol Soc*. <https://doi.org/10.1002/qj.49712757103>
- Walsh K, Lavender S, Scoccimarro E, Murakami H (2013) Resolution dependence of tropical cyclone formation in CMIP3 and finer resolution models. *Clim Dyn* 3–4(40):585–599. <https://doi.org/10.1007/s00382-012-1298-z>
- Walsh KJE, Camargo SJ, Vecchi GA, Daloz AS, Elsner J, Emanuel K, Horn M, Lim Y-K, Roberts M, Patricola C, Scoccimarro E, Sobel AH, Strazzo S, Villarini G, Wehner M, Zhao M, Kossin JP, LaRow T, Oouchi K, Schubert S, Wang H, Bacmeister J, Chang P, Chauvin F, Jablonowski C, Kumar A, Murakami H, Ose T, Reed KA, Saravanan R, Yamada Y, Zarzycki CM, Vidale PL, Jonas JA, Henderson N (2015) Hurricanes and climate: the U.S. CLIVAR Working Group on Hurricanes. *Bull Am Meteorol Soc*. <https://doi.org/10.1175/BAMS-D-13-00242.1>
- Wang X, Jiang H (2019) A 13-year global climatology of tropical cyclone warm-core structures from airs data. *Monthly Weather Rev* 147(3):773–790
- Wehner M, Prabhat P, Reed KA, Stone D, Collins WD, Bacmeister J (2015) Resolution Dependence of Future Tropical Cyclone Projections of CAM5.1 in the U.S. CLIVAR Hurricane Working Group Idealized Configurations. *J Clim*. <https://doi.org/10.1175/JCLI-D-14-00311.1>
- WMO (2023) Les Catastrophes Météorologiques Se Sont Multipliées Au Cours des 50 Dernières Années, Causant Plus de Dégâts, Mais Moins de Décès. <https://public.wmo.int/fr/medias/communiqu%C3%A9s-de-presse/les-catastrophes-m%C3%A9t%C3%A9orologiques-se-sont-multipli%C3%A9es-au-cours-des-50>. Accessed 2023-02-22
- Wu X, Reed KA, Callaghan P, Bacmeister JT (2022) Exploring western north pacific tropical cyclone activity in the high-resolution community atmosphere model. *Earth Space Sci* 9(1):2021–001862
- Zarzycki CM, Ullrich PA (2017) Assessing sensitivities in algorithmic detection of tropical cyclones in climate data. *Geophys Res Lett*. <https://doi.org/10.1002/2016GL071606>
- Zarzycki CM, Ullrich PA, Reed KA (2021) Metrics for evaluating tropical cyclones in climate data. *J Appl Meteorol Climatol*. <https://doi.org/10.1175/JAMC-D-20-0149.1>
- Zhang W, Villarini G, Scoccimarro E, Roberts M, Vidale PL, Vanniere B, Caron L-P, Putrasahan D, Roberts C, Senan R, Moine M-P (2021) Tropical cyclone precipitation in the HighResMIP atmosphere-only experiments of the PRIMAVERA Project. *Clim Dyn*. <https://doi.org/10.1007/s00382-021-05707-x>
- Zhao M, Held IM, Lin S-J (2012) Some counterintuitive dependencies of tropical cyclone frequency on parameters in a GCM. *J Atmos Sci*. <https://doi.org/10.1175/JAS-D-11-0238.1>

Publisher's Note Springer Nature remains neutral with regard to jurisdictional claims in published maps and institutional affiliations.